Nano Research

Open Access

Research Article

Cerium-doped zinc oxide anchored halloysite nanoclays as skin management system for photoprotection and radiative cooling

Xiangyu Chen[1], Yuwei Qiu[1], Shuiqing Zhou[1], Chuangchi Ma[1], Hong Li[1,2], and Mingxian Liu[1,2] ✉

[1] *Department of Materials Science and Engineering, College of Chemistry and Materials Science, Jinan University, Guangzhou 511443, China*
[2] *Engineering Research Center of Artificial Organs and Materials, Ministry of Education, Guangzhou 510632, China*

Cite this article: *Nano Research*, **2026**, *19*, 94908443. https://doi.org/10.26599/NR.2026.94908443

ABSTRACT: Sunscreens are crucial for skin health by protecting against the harmful effects of ultraviolet (UV) radiation. To overcome persistent limitations of irritation and discomfort in existing formulations, a high-performance radiative cooling sunscreen, CZHR, has been strategically designed. This formulation synergistically integrates cerium-doped zinc oxide (Ce-ZnO) and halloysite nanotubes (HNTs) to achieve dual UV protection and skin cooling. As a nanocarrier, HNTs effectively regulate the particle size, morphology, and oxygen vacancies of Ce-ZnO, significantly enhancing UV protection and catalytic activity. Resveratrol is further incorporated to improve UV resistance and pathogen inhibition. The resulting CZHR-based Pickering emulsion exhibits excellent UV shielding, high solar reflectance (0.73), and infrared emissivity (0.87). *In vitro* and *in vivo* tests show efficacy in alleviating UV-induced cellular damage and inhibiting biofilm formation. Notably, compared to commercial products, the CZHR sunscreen reduces skin temperature by an additional 1.7–2.9 °C. Biosafety evaluation confirms non-irritating property and negligible skin penetration. This thermal management system represents a promising platform for advanced photoprotection and radiative cooling.

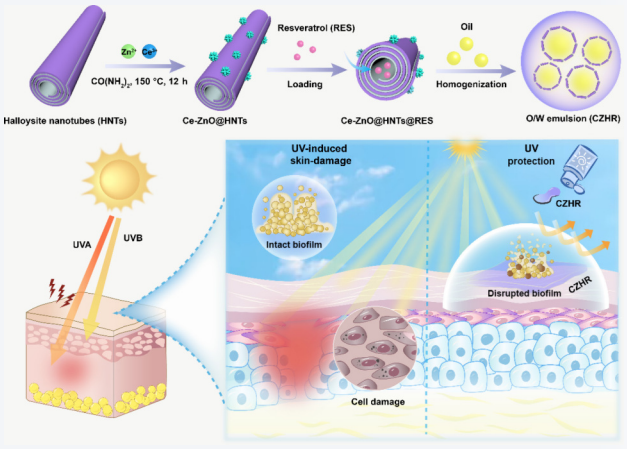

KEYWORDS: halloysite nanoclays, sunscreen, photoprotection, radiative cooling, ultraviolet (UV) radiation

1 Introduction

Excessive or prolonged exposure to ultraviolet (UV) radiation can lead to various harmful effects, including sunburn, photoaging, oxidative stress, and skin cancer [1, 2]. Especially, increased UV exposure resulting from ozone depletion is likely to worsen this global issue [3, 4]. UVA (400–320 nm) penetrates both the epidermis and dermis, resulting in oxidative stress and prolonged tanning [5]. UVB (320–290 nm) directly damages DNA, raising the risk of mutations that contribute to skin aging and cancer [6]. To mitigate skin risks from direct sunlight, sunscreens are commonly used, especially for outdoor workers. Organic sunscreens (e.g., avobenzone) can absorb UV radiation and convert it into heat energy, so they face issues of photodegradation and potential phototoxicity [7]. In contrast, inorganic sunscreens are generally non-toxic, provide broad-spectrum protection, and do not generate additional heat, making them a more favorable option [8]. Nevertheless, traditional sunscreens are ineffective in alleviating human discomfort caused by visible light and near-infrared radiation in hot outdoor environments [8]. Furthermore, the high density and surface energy of micro-nano zinc oxide (ZnO) and titanium dioxide (TiO_2) make them susceptible to agglomeration and sedimentation, which can compromise their UV filtering efficiency [1, 9]. Therefore, developing a sunscreen that combines UV protection with cooling functionality presents a significant challenge.

ZnO is a well-known light-responsive material and antimicrobial agent approved by the U.S. Food and Drug Administration (FDA) [10]. It is commonly used in commercial sunscreens, providing broad-spectrum UV protection [11]. To enhance the UV absorption of ZnO, element doping may be a feasible strategy [12, 13]. For example, cerium (Ce) dopants exhibit multiple oxidation states, and doping into metal oxides can introduce defect structures and active sites [14]. More importantly, Ce ions are

Received: December 25, 2025; **Revised:** January 13, 2026
Accepted: January 13, 2026

✉Address correspondence to liumx@jnu.edu.cn

confirmed to serve as the electron acceptor to facilitate the charge separation and reduce electron-hole pair recombination [15], which thus propels antimicrobial properties derived from photocatalytic performance. Unfortunately, a significant drawback of ZnO nanoparticles is their tendency to agglomerate, so they may form a white film, causing noticeable "false whitening" in the skin. Therefore, an optimal formulation based on ZnO still needs to be developed to erase these disadvantages.

Halloysite nanotubes (HNTs), a type of natural clay material, is widely distributed in nature and is characterized by a unique hollow tubular structure [16]. The white waxy appearance and layered aluminosilicate structure indicate reflective and scattering properties, making HNTs natural skin protectors [17]. As a member of mineral medicine, HNTs is the main component of Chishizhi, which has been used for the treatment of skin and gastrointestinal diseases for thousands of years in Asia. The outer surface of HNTs consists of silicon-oxygen tetrahedra bonded by Si-O-Si bonds, whereas the inner surface comprises aluminum-oxygen octahedra featured by Al–OH bonds [18]. The abundant Si-O, Si-O-Si and Al-O chemical bonds may enable HNTs to achieve high emissivity within the 8–13 μm atmospheric window [19]. HNTs serve as an ideal support for the *in situ* growth of metals and metal oxide nanoparticles, leading to tunable particle size, tailorable morphology, enhanced dispersity, and improved activity, thereby facilitating applications related to catalysis, adsorption, and chemical reactions [20, 21]. Moreover, HNTs' lumen can be containers for loading active ingredients and achieving sustained release [22]. For example, bioactive packaging films with sustained antimicrobial and antioxidant activity were developed using HNTs loaded with carvacrol as a sustained release system [23, 24]. Also, the rod-like HNTs is suitable as interfacial stabilizers in Pickering emulsions, which has been used to design a sunscreen in our previous work [25]. Compared to the earlier study, the present investigation explores novel applications of nanoclay-based photoprotective materials, specifically their roles in thermal management and skin repair.

Herein, an *in situ* synthesis strategy of Ce-doped ZnO on the outer surface of HNTs (Ce-ZnO@HNTs) was proposed with an inner cavity loaded with resveratrol (RES) for UV resistance and skin protection (Scheme 1). Ultra-small Ce-doped ZnO nanoparticles (~ 9 nm) were anchored on the surface of HNTs using the solvothermal method to avoid particle agglomeration and improve catalytic activity. Then, Ce-ZnO@HNTs were formulated into a Pickering emulsion (CZHR sunscreen) using liquid paraffin. The sunscreen provides excellent UV shielding and radiative cooling properties that reduce UV-induced skin damage, oxidative stress, and heat discomfort. In addition, due to the sustained release of RES, the sunscreen inhibits biofilm formation by disrupting the redox balance of bacterial membranes without damaging normal skin cells. Together, these results demonstrate that CZHR sunscreen can be used as a biocompatible skin management system for photoprotection and radiative cooling, highlighting good commercial potential in the sunscreen market.

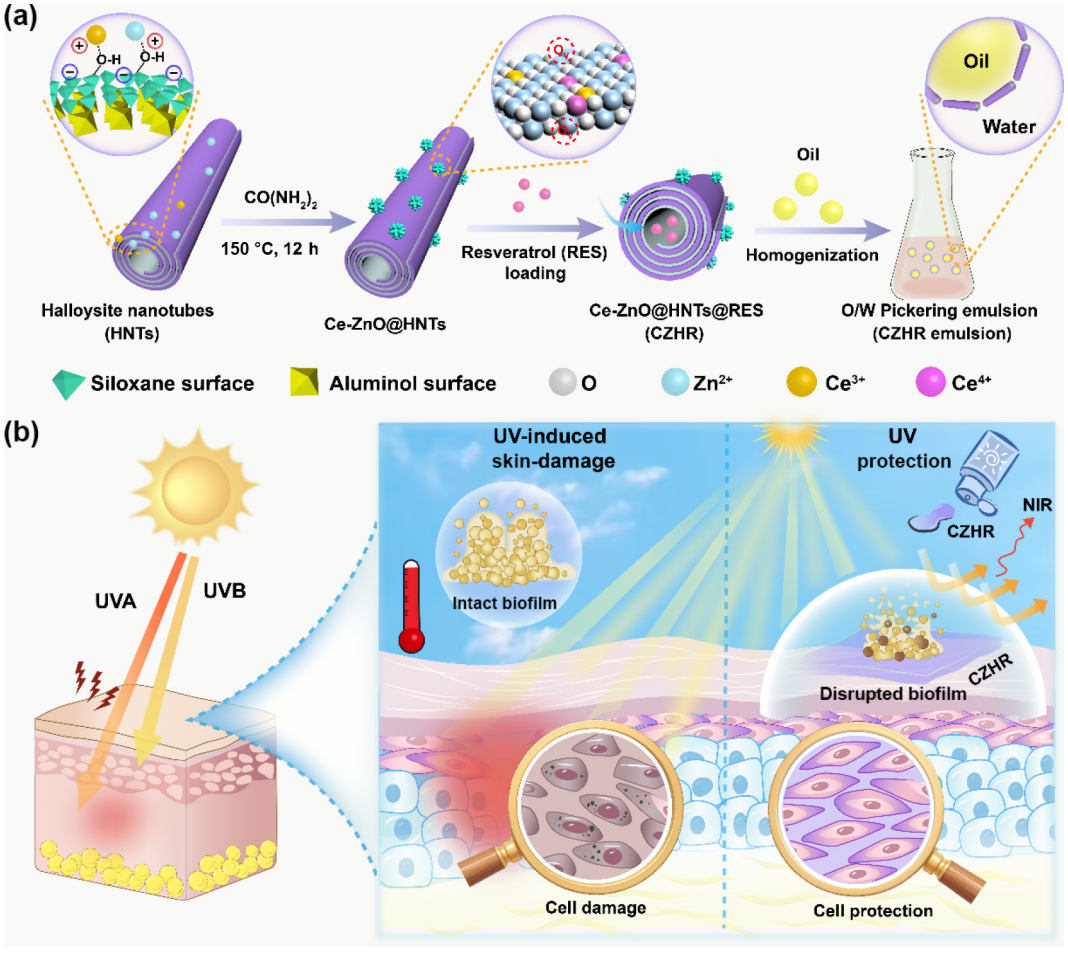

Scheme 1 Schematic diagram of the *in situ*-synthesis of Ce-ZnO on HNTs and the preparation of CZHR Pickering emulsion for UV protection, skin thermal management, and biofilm inhibition.

2 Experimental

2.1 Materials

High-purity HNTs were supplied by Guangzhou Runwo Materials Technology Co., Ltd. $Ce(NO_3)_3{\cdot}6(H_2O)$, dihydro-rhodamine (DHR), polyvinyl alcohol (PVA), hexadecyltrimethoxysilane (HDTMS), Nile Red and fluorescein isothiocyanate (FITC) were purchased from Shanghai Macklin Biochemical Co., Ltd., China. The ethanol was purchased from Tianjin Damao Chemical Reagent Co., Ltd., and the urea from Tianjin Fuchen Chemical Reagent Co., Ltd., China. Resveratrol, $Zn(CH_3COO)_2{\cdot}2H_2O$, and liquid paraffin were purchased from Shanghai Yien Chemical Technology Co., Ltd., China. Commercial sunscreen (Anessa, sun protection factor (SPF): 50+) was purchased from Shiseido, Japan Co., Ltd. All cell culture reagents were ordered from Thermo Fisher Scientific Inc. (USA). Cell culture flasks and plates were purchased from Corning Inc. (USA). Molecular and cell biology reagents were purchased from the relevant companies (specified when mentioned later).

2.2 *In situ* synthesis of Ce-ZnO on HNTs

ZnO@HNTs, with varying Ce dopant concentrations, were synthesized via a solvothermal method. In brief, a homogeneously dispersed ethanol suspension of HNTs was prepared. Subsequently, a 50 mL ethanol solution containing 0.390 g $Zn(CH_3COO)_2{\cdot}2H_2O$ and 0.125 g urea was added dropwise to 50 mL of the HNTs dispersion. Varying amounts of $Ce(NO_3)_3{\cdot}6H_2O$ were then introduced as the Ce dopant, resulting in final Ce concentrations of 0, 1.56 mol%, 2.59 mol%, 5.31 mol%, 8.19 mol%, and 11.24 mol% relative to Zn (final concentration: 0.42 wt% HNTs). The mixture was sonicated for 30 min and then stirred vigorously for an additional 30 min. Immediately after stirring, the mixture was transferred to a polytetrafluoroethylene reaction vessel and subjected to hydrothermal treatment at 150 °C for 12 h. The product was centrifuged at 6000 rpm for 8 min, washed three times with ethanol, and then lyophilised to obtain Ce-ZnO@HNTs for further use.

2.3 Preparation of Ce-ZnO@HNTs@RES (CZHR)

An ethanol dispersion of Ce-ZnO@HNTs (0.1 wt%) was prepared by adding 1 mM of RES and stirring well. The mixture underwent three vacuum cycles to facilitate RES loading into the HNTs lumens (0.5 h vacuum, 0.5 h ambient pressure). After three cycles, the Ce-ZnO@HNTs@RES was washed three times by centrifugation in ethanol to remove the remaining RES. It was then freeze-dried to obtain Ce-ZnO@HNTs@RES.

2.4 CZHR Pickering emulsion preparation

The aqueous dispersion of Ce-ZnO@HNTs@RES was used as the aqueous phase, while liquid paraffin served as the oil phase. The water-oil mixture was sonicated and homogenized to produce an oil-in-water CZHR Pickering emulsion. Polyvinyl alcohol aqueous solution (final concentration: 2.5 wt%) was added to the emulsion to enhance the film-forming properties of the emulsion. To further investigate Ce-ZnO@HNTs@RES as stabilizers at the oil-water interface, the oil phase was stained with Nile Red (excitation/emission wavelengths of 552/636 nm), and HNTs were labeled with FITC (excitation/emission wavelengths of 490/520 nm). Fluorescence images of the Pickering emulsion were captured using fluorescence microscopy (Axio Vert. A1, Zeiss, Germany).

2.5 Characterization

Transmission electron microscopy (TEM) (JEM−1400 Flash, JEOL Ltd., Japan) and scanning electron microscopy (SEM) (SU1000, HITACHI, Japan) images were employed to characterize the size, morphology, structure, and elemental distribution of Ce-ZnO@HNTs. An X-ray diffraction (XRD) instrument (MiniFlex-600, Rigaku Corporation, Japan) was used to analyze the crystalline structure of HNTs, ZnO, and Ce-ZnO@HNTs with a scan rate of 5° min^{-1} ranging from 5° to 80°. X-ray photoelectron spectroscopy (XPS) was measured by an XPS instrument (ESCA-LAB250Xi, Thermo Fisher Scientific Ltd., USA). The UV absorption and transmission spectra of various materials were measured from 200 to 600 nm using a UV−vis spectrophotometer (UV-2550, Suzhou Shimadzu Instrument Ltd., China) at 0.5 nm intervals. The Ce-ZnO content was analyzed by a thermogravimetric analysis (TGA) instrument (Mettler Toledo, Switzerland) from 30 to 700 °C at a heating rate of 10 °C/min under an N_2 atmosphere. The size distribution and zeta potential analysis were carried out using a Nano ZS zeta potential analyzer (Malvern Instruments Co., UK). A contact angle analyzer (DSA 100, DataPhysics, OCA-25, Germany) was utilized to analyze the water wettability of HDTMS-modified Ce-ZnO@HNTs. The emulsion morphology was observed using a polarized microscope (BX51, Olympus, Japan) at 500× magnification.

2.6 *In vitro* UV protection effect

HNTs emulsion, Ce-ZnO@HNTs sunscreen, commercial sunscreen, and CZHR sunscreen were applied on high-transmittance quartz slides with a spreader to prepare a 100 μm sunscreen film. The test samples were covered on the UV intensity indicator card, and the blank quartz slide was used as a control. The indicator card was photographed after 5 min of exposure to UV light.

For the DHR assay, the above-prepared test samples were covered with a 96-well plate containing an aqueous solution of DHR at a concentration of 5 ng/mL. After exposure to UV light, UV-induced reactive oxygen species (ROS) production was tested by measuring the plate's fluorescence intensity at specific time points using an excitation/emission wavelength of 500/536 nm.

The samples' transmittance to UVA and UVB radiation was measured using a UV transmittance analyzer (UV2000F, Labsphere, USA). The UVA transmittance was determined within the wavelength range of 320–400 nm, and the UVB transmittance was measured within the wavelength range of 280–320 nm.

SPF determination: Each sample was uniformly coated on a high-transmittance quartz slide at a concentration of 2 mg/cm^2 using an applicator, then left to dry naturally in an undisturbed environment to allow the emulsion to form a uniform film. The transmittance and absorbance of the samples were measured in the range of 280–400 nm using a UV transmittance analyzer (UV2000F, Labsphere, USA), and the SPF value of each sample was calculated from the spectral data.

2.7 Measurement of radiative cooling performance

The reflectivity (R) and transmissivity (T) were measured using a UV−Vis−near-infrared (NIR) spectrometer (UV3600, Shimadzu, Japan) in the range of 0.25–2.5 μm with an integrating sphere, while in the mid-infrared (MIR) range (2.5–25 μm) using a Fourier transform infrared spectroscopy (FTIR) spectrometer (Nicolet iS50, ThermoScientific, USA) equipped with a diffuse gold integrating sphere (Pike Technologies, USA).

The definition of average solar reflectivity (R_{solar}, 0.3–2.5 μm) of the sample is calculated with Eq. (1).

$$R_{\text{solar}} = \frac{\int_{0.3}^{2.5} I_{\text{solar}}(\lambda) R(\lambda) \, \mathrm{d}\lambda}{\int_{0.3}^{2.5} I_{\text{solar}}(\lambda) \, \mathrm{d}\lambda} \quad (1)$$

Here λ is the wavelength, I_{solar} (λ) is the ASTMG173-03 AM1.5 Global Tilt spectrum, and $R(\lambda)$ is the spectral reflectivity of the surface.

The definition of average atmospheric window emissivity of the sample is calculated with Eq. (2).

$$\varepsilon_1 = \frac{\int_8^{13} I_{\text{bb}}(T,\lambda) \, \varepsilon(\lambda) \, \mathrm{d}\lambda}{\int_8^{13} I_{\text{bb}}(T,\lambda) \, \mathrm{d}\lambda} \quad (2)$$

Here $I_{\text{bb}}(T, \lambda)$ is the spectral irradiance emitted by a blackbody at temperature T (25 °C), and $\varepsilon(\lambda)$ is the spectral thermal emissivity of the surface.

Additionally, CZHR sunscreen was applied to Cu plates. The plates were exposed to simulated sunlight from a xenon lamp (1 sun), and surface temperatures were monitored using an infrared camera. In a separate experiment, CZHR sunscreen was applied to skin. The skin's surface temperature was monitored using an infrared camera during outdoor testing on a rooftop in Guangzhou (113°15′53″ E, 23°06′32″ N) in June 2025.

2.8 Cell culture, UV-induced cell death, and DNA damage analysis

The human immortalized keratinocyte cell line (HaCaT) was obtained from the American Type Culture Collection (ATCC, USA) and cultured in Dulbecco's modified Eagle's medium (DMEM) supplemented with 10% fetal bovine serum and 1% Penicillin–Streptomycin. HaCaT cells were seeded at a low density of 2×10^3 to 4×10^3 cells/mL in 12- or 24-well plates for live/dead staining, apoptosis analysis by flow cytometry, or immunofluorescence. For 3-(4,5-dimethylthylthiazol-2-yl)-2,5-diphenyltetrazolium bromide (MTT) cell viability assays, the cells were in 96-well plates. The plates were incubated at 37 °C in a 5% CO_2 and 95% air atmosphere until cell attachment was confirmed. Subsequently, the culture medium was discarded, and PBS was added to just cover the bottom of the wells. Quartz slides coated with the test sunscreen were then placed over the corresponding wells. The cells were irradiated with a UV lamp positioned 10 cm above the bottom of the plate for 5 min. After irradiation, fresh culture medium was added, and the cells were incubated for an additional 6 h before harvesting for flow cytometry analysis and immunofluorescence staining to assess DNA damage. The cells were further cultured for 24 h post-irradiation, after which live/dead staining and cell viability assays were performed.

2.9 *In vitro* antibacterial assays

The bacteria were randomly divided into eight groups: PBS UV (+/−), HNTs UV (+/−), Ce-ZnO UV (+/−), and Ce-ZnO@HNTs UV (+/−), where "UV (+)" and "UV (−)" indicate the UV lamp (Philips, 311 nm, 9 W) being turned on and off, respectively. *Escherichia coli* (*E. coli*) and *Staphylococcus aureus* (*S. aureus*) were activated by the overnight culture at 37 °C in Luria-Bertani (LB) broth. The diluted bacterial suspensions were mixed with different materials (500 μg/mL) and incubated at 37 °C. Afterwards, the diluted suspension was spread evenly onto agar plates and incubated at 37 °C for 16 h. Colonies were photographed, and the bacterial viability was calculated.

2.10 Evaluation of anti-biofilm

The bacterial suspension (300 μL, 1×10^7 colony-forming units (CFU)/mL) and a Ce-ZnO@HNTs dispersion (300 μL) were added to 24-well plates. After UV irradiation (10 min), the plates were incubated at 37 °C for 36 h to form biofilms, and the medium was replaced every 24 h. Subsequently, the biofilms were carefully washed three times with PBS and fixed with 4% paraformaldehyde for 30 min. After staining with 0.1% crystal violet solution and washing, the biofilm images were photographed. Biofilms were quantified by dissolving crystal violet in 400 μL of ethanol and measuring the absorbance at 570 nm using a microplate reader (Elx800, BioTek, USA). To observe the 3D structure of biofilms, biofilms formed in confocal petri dishes were obtained as described above and stained with acridine orange (AO) and propidium iodide (PI) staining solution for 30 min in the dark. Finally, 3D images of the biofilms were acquired using a confocal laser scanning fluorescence microscope (CLSM, LSM800, Zeiss, Germany). The microscopic morphology of biofilms and bacteria after different treatments was observed by SEM. Biofilms were formed on cell slides (9 mm) at the bottom of 48-well plates. The remaining steps were performed as previously described. The biofilms were fixed with 2.5% glutaraldehyde for 2 h at 4 °C. The samples were then dehydrated in a graded ethanol series (30%, 50%, 70%, 80%, 90%, and 100%) for 15 min each. Finally, the samples were observed using a field emission SEM (FESEM) (ULTRA55, Zeiss, Germany).

2.11 *In vivo* skin penetration assessment

Female Kunming (KM) mice (6–8 weeks old) were housed at Guangdong Huawei Testing Co., Ltd. and nimal procedures were performed in accordance with the protocols of its ethics committee, with free access to food and water throughout the study. One day in advance, the dorsal hair of the mice was carefully removed by an electric razor and depilatory cream (Veet, France) to ensure there was no skin damage. Before the experiment, the backs of the mice were cleaned with a PBS buffer solution. Then, 0.1 mg/mL of FITC-labelled ZnO and Ce-ZnO@HNTs were applied topically to the mouse skin. After 6 h of free movement in a dark environment, skin tissue samples were taken and fixed with 4% paraformaldehyde before being prepared as frozen sections. The tissue sections were then visualized using a fluorescence microscope (Observer Z1, Germany). ZnO nanoparticles (30–50 nm) were used as model small particles to investigate the effect of particle size on skin permeability.

2.12 Evaluation of CZHR skin adhesion *in vivo*

FITC-labeled CZHR Pickering emulsion was applied to the dorsal hair of the mice. To assess CZHR retention, mice were individually housed and imaged *in vivo* using an *in vivo* imaging system (IVIS) fluorescence imager (IVIS Lumina Series III, PerkinElmer, USA) at various time points. To evaluate the water resistance and mechanical removal of CZHR, the treated area was wiped with a wet towel and washed under running water, respectively.

2.13 Safety evaluation

For the cytotoxicity assay, HaCaT cells were seeded into 96-well plates at a density of 2×10^3 cells per well, and after attachment, different concentrations of Ce-ZnO@HNTs and CZHR were added. After incubation, cell viability was assessed using the MTT assay. The dorsal skin of mice was used for the skin irritation and inflammation test. CZHR emulsion was applied to the dorsal skin of mice once daily for 7 days. On day 8, tissue samples of the skin,

heart, liver, spleen, lungs, and kidneys were collected, washed with PBS, fixed with 4% paraformaldehyde, and processed for histological examination according to hematoxylin and eosin (H&E) staining protocols.

2.14 *In vivo* anti-UV effect

The dorsal skin of the mice was divided into six regions (1 cm × 1 cm), which were treated with PBS, HNTs emulsion, Ce-ZnO@HNTs sunscreen, commercial sunscreen, and CZHR sunscreen, respectively. The remaining skin was covered with blackout cloth. Subsequently, the dorsal skin was exposed to a UV lamp (Philips, 311 nm, 9 W) for 15 min. Skin tissues were collected for histological analysis and histopathological examination after irradiation.

For H&E and Masson trichrome staining, the skin samples were cut into 4 μm-thick sections and stained using standard protocols. Specifically, the sections were deparaffinized with xylene, rehydrated through a gradual ethanol series, and then stained using the staining kit (Wuhan Servicebio Biotechnology Co., Ltd., China). Epidermal thickness and keratin content were analyzed using ImageJ software (National Institutes of Health, USA).

For immunohistochemistry, the skin sections were deparaffinized by xylene, rehydrated through a graded series of ethanol, antigen retrieval was performed for 30 min in citrate buffer (0.1 M, pH 6), and blocked for endogenous peroxidase activity. Sections were incubated with anti-IgE (1:200, M113908, Wolcavi, China) diluted in serum solution overnight at 4 °C. Next, sections were incubated with secondary antibodies. The secondary antibodies used were: horseradish peroxidase (HRP) goat anti-mouse IgG (1:200, GB23301, Servicebio, China). Finally, fluorescent images of the stained sections were captured by fluorescence microscopy (Axio Observer 3, ZEISS, Germany).

For immunofluorescence, skin tissue sections (4 μm thickness) were prepared. Briefly, after rewarming from storage conditions, the sections were subjected to the following sequential steps: secondary fixation (4% paraformaldehyde), permeabilization (0.1% Triton X-100/PBS), and blocking. Subsequently, sections were incubated with primary antibodies at 4 °C overnight. The primary antibodies used were: Anti-Phospho-H2AX (1:300, GB111841-100, Servicebio, China) and anti-8-OHdG (1:200, sc-66036, Santa Cruz, US). Sections were washed with PBS and then incubated with secondary antibodies at room temperature. The secondary antibodies used were: Alexa Fluor 488 goat anti-rat IgG (1:400, GB25303, Servicebio, China) and CY3 goat anti-mouse IgG (1:300, GB21401, Servicebio, China). After incubation, the sections were washed with PBS and counterstained with 4',6-diamidino-2-phenylindole (DAPI) (C1005, Beyotime, China) for 10 min to label nuclei. Finally, these samples were imaged with a fluorescence microscope.

2.15 Statistical analysis

The data are presented as mean ± standard deviation (SD) and represent the results of multiple independent experiments. All experiments were repeated at least 3 times. Statistical analyses were performed using GraphPad Prism 7 (GraphPad Software, Inc., USA) and Origin 2021 (OriginLab, USA). Comparisons between groups were analyzed using a two-tailed Student's t-test, while comparisons within groups were analyzed using one-way ANOVA with Tukey's post-hoc test. $P < 0.05$ was considered statistically significant.

3 Results and discussion

3.1 Confined-synthesis and characterization of CZHR

Aluminosilicate clays widely act as natural inorganic UV filters in daily life [26]. UV–Vis absorption curves reveal that, compared to the sheet-like particles of kaolin and montmorillonite, the cylindrical surfaces of HNTs and attapulgite exhibit enhanced scattering and reflection of light below 400 nm (Fig. S1 in the Electronic Supplementary Material (ESM)). HNTs is a naturally occurring, hollow, tubular clay mineral composed of aluminosilicate layers, showing promising application in the biomedicine area. The unique chemical composition, structure, and adsorption capacity of HNTs are utilized to synergistically enhance UV-shielding capabilities by selectively modifying and loading commercial UV filters, providing a practical strategy for sunscreen formulation (Fig. S2 in the ESM).

The *in-situ* synthesis of Ce-doped ZnO on the HNTs was conducted using a simple solvothermal method (Fig. 1(a)). The abundant –OH groups and negatively charged outer surface of HNTs facilitate the anchoring of Zn and Ce ions, providing numerous nucleation sites for the growth of ZnO [27]. Figure S3 in the ESM displays the XRD patterns of ZnO@HNTs with varying Ce mole fractions (x). The shift of diffraction peaks towards lower 2θ angles with increasing Ce content indicates lattice expansion, which is attributed to the partial substitution of Zn (ionic radius 0.74 Å) by Ce (ionic radius 1.01 Å), thus confirming the successful doping. Previous studies have shown that Ce-doped ZnO enhances photocatalyst light absorption by improving carrier transport and adjusting the bandgap width [12, 28].

The microstructure of Ce-ZnO@HNTs was analyzed using TEM (Fig. 1(b)). It was found that ultra-small flower-like Ce-doped ZnO nanocrystals formed on the outer surface of HNTs. The SEM also confirmed that Ce-ZnO nanoparticles covered the smooth surface of HNTs (Fig. 1(c) and Fig. S4 in the ESM). The Si-OH active sites on HNTs' surface significantly lowered the nucleation barrier, favoring heterogeneous ZnO nucleation on the HNTs' outer surface over homogeneous nucleation in the solvent. Furthermore, the agglomeration of Ce-ZnO nanocrystals without HNTs suggests the HNTs' spatial confinement effect (Fig. S5 in the ESM). As shown in the TEM images of Ce-ZnO@HNTs, the addition of water resulted in suppressed ZnO nucleation on the surface of HNTs (Fig. S6 in the ESM). This is possibly because water molecules disturb the crystallinity degree of ZnO by altering the solvent polarity and influencing the competitive adsorption of metal ions with HNTs, thereby interfering with the crystal growth process.

The high-resolution transmission electron microscopy (HRTEM) image (Fig. 1(d)) reveals distinct lattice fringes in the Ce-ZnO nanocrystals. The calculated interplanar spacings of 0.290, 0.261, 0.185 and 0.301 nm correspond to the (100), (002), (102) planes of ZnO and the (111) plane of CeO_2, respectively. The selected area electron diffraction (SAED) pattern of Ce-ZnO@HNTs reveals a polycrystalline structure (Fig. 1(e)). Energy-dispersive spectroscopy (EDS) mapping images indicate that Ce-ZnO nanocrystals are uniformly distributed on the surface of HNTs (represented by Al and Si elements) (Fig. 1(f)). Particle size distribution statistics demonstrate that the size of Ce-ZnO@HNTs increases to 747.5 nm from 309.8 nm of HNTs (Fig. S7 in the ESM).

Upon Ce doping, the size of ZnO nanocrystals decreased to

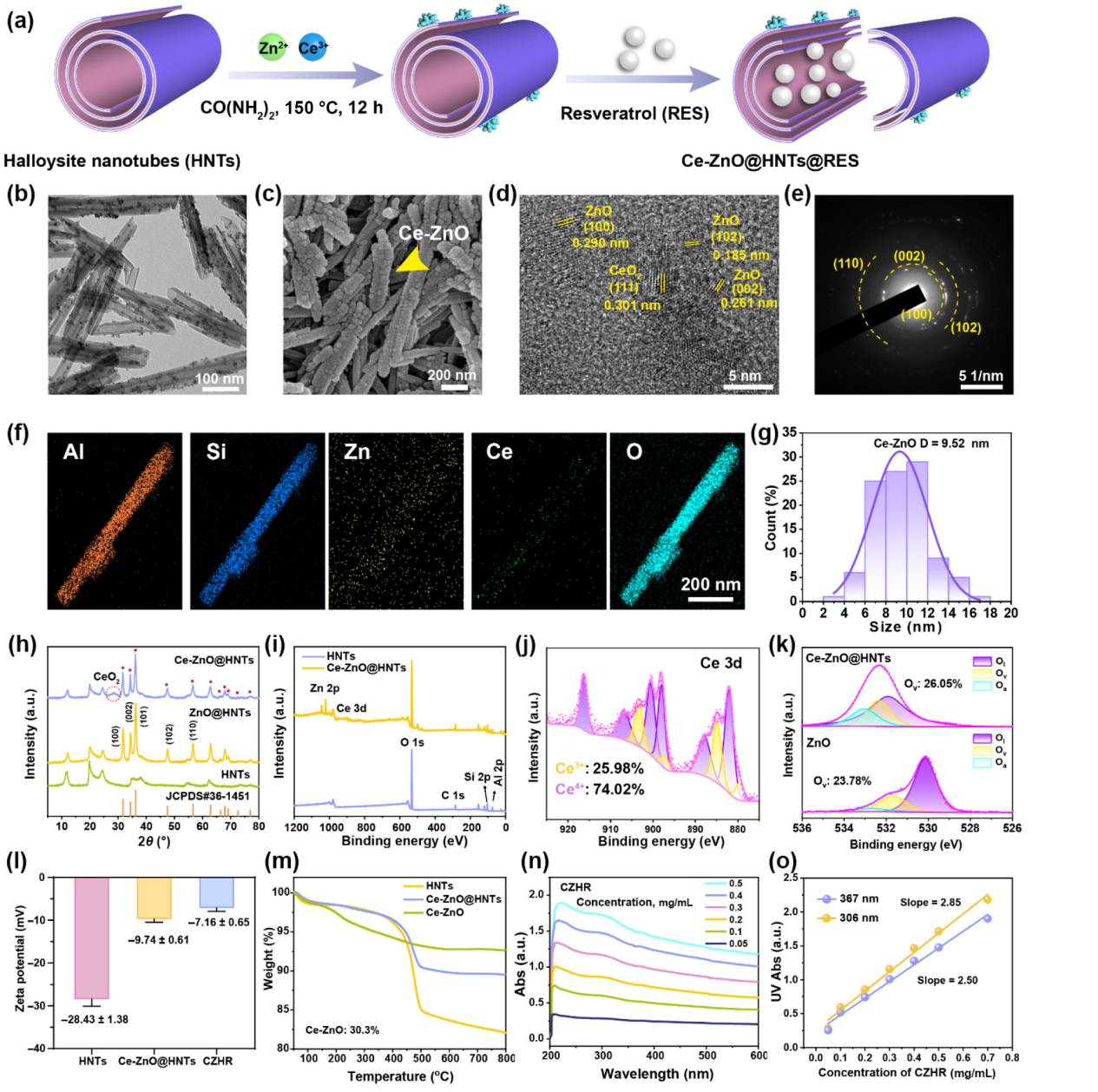

Figure 1 Synthesis and characterization of CZHR. (a) Schematic diagram of the synthesis process. (b) TEM image. (c) SEM image. (d) HRTEM image. (e) SAED patterns. (f) Elements mapping. (g) Particle size distribution. (h) XRD patterns. (i) Wide-range XPS spectra of Ce-ZnO@HNTs. (j) Ce 3d XPS spectra and (k) O 1s XPS spectra. (l) Zeta potential in aqueous dispersion. The data are presented as the mean ± SD, n = 3. (m) TGA curves. (n) UV absorption curves and (o) corresponding concentration-absorbance linear fitting of CZHR.

9.52 nm (Fig. 1(g)). The reduction in particle size may be attributed to the formation of Ce-O-Zn, which influences on the nucleation and growth processes of ZnO [29, 30]. The UV absorption performance is size-dependent, with a more pronounced quantum confinement effect observed in smaller ZnO particles. XRD patterns of Ce-ZnO@HNTs reveal distinct diffraction peaks at 31.6°, 34.3°, 36.1°, 47.5°, and 56.6°, corresponding to the (101), (002), (110), (201), and (303) crystal planes, respectively, indicating a hexagonal wurtzite structure of ZnO (JCPDS #36-1451). Additionally, a characteristic peak at 28.6° confirms the cubic fluorite structure of CeO_2 (JCPDS #34-0394) (Fig. 1(h)). The characteristic peaks of the Ce-ZnO@HNTs sample for the (100), (002), and (101) planes exhibit a distinct shift to lower angles compared to those of ZnO@HNTs, implying significant lattice expansion of ZnO resulting from Ce doping [31]. The coexistence of shifted ZnO peaks and the emergence of CeO_2 (111) diffraction peaks indicate that the sample is in a state of over-doping. While a portion of Ce ions successfully substitute Zn sites in the wurtzite lattice (confirmed by lattice expansion), the excess Ce segregates at the grain boundaries to form CeO_2 secondary phases. This unique structure of "doped matrix + heterojunction" is favorable for modulating the electronic structure, interfacial behavior, charge transport, and catalytic/optoelectronic properties of materials.

The chemical bonds and electronic states of Ce-ZnO@HNTs were characterized by XPS. The full XPS spectrum confirmed the presence of C, O, Al, Si, Ce, and Zn in Ce-ZnO@HNTs, with an actual Ce doping concentration of 4.88% (Fig. 1(i) and Fig. S8(a) in the ESM). The binding energy of Zn 2p exhibited a slight blue shift

(Fig. S8(b) in the ESM), indicating the alteration of electron density at the Zn sites upon Ce doping and the interfacial interaction with the HNTs. The Ce 3d XPS spectrum (Fig. 1(j)) reveals the chemical valence state of the rare earth element, with a Ce^{3+} percentage of 25.98% in the Ce-ZnO@HNTs. The presence of Ce^{3+} in nanocrystals, reflecting oxygen vacancies (Ov) defects, underpins catalytic activity. The switching property of the redox couple Ce^{4+}/Ce^{3+} can be applied based on the transfer of photogenerated electrons from the conduction band of ZnO to Ce^{4+}, followed by reduction of Ce (IV) to Ce (III), decreasing the rate of the electron-hole recombination [32]. The O 1s spectra of ZnO displayed three peaks at 530.18, 531.68, and 532.78 eV, corresponding to lattice oxygen, O_v, and surface oxygen, respectively. In Ce-ZnO@HNTs, these peaks shifted to higher binding energies (531.88, 532.38, and 533.08 eV), indicating charge transfer within the oxygen species (Fig. 1(k)). The O_v proportion increased to 26.05% in Ce-ZnO@HNTs, compared to 23.78% in ZnO, suggesting that HNTs-mediated interface regulation combined with Ce incorporation effectively promotes surface Ov formation on ZnO [33, 34]. The presence of O_v in the crystal lattice and defect sites on the surface of Ce-ZnO contributes to tailoring the band structure and enhancing UV absorption.

Despite the Ce-ZnO nanoparticles carrying a positive charge, Ce-ZnO@HNTs still exhibit a negative charge, with a value of −9.74 ± 0.61 mV. The loading of RES into the lumen of Ce-ZnO@HNTs does not significantly alter their charge properties, which remain at −7.16 ± 0.65 mV, conferring excellent dispersibility of the composite in water (Fig. 1(l)). The Ce-ZnO content in Ce-ZnO@HNTs, as measured by TGA, is 30.3% (Fig. 1(m)). As shown in Fig. 1(n), RES loading reduced the maximum absorption wavelength to 306 nm (close to that of DNA and RNA at 260 nm), indicating that RES enhances the UV genotoxicity protection capacity of Ce-ZnO@HNTs. The linear fit of concentration-maximum absorbance reveals that the slopes of CZHR at 367 and 306 nm are 2.85 and 2.50, respectively, suggesting a further enhancement of the UV absorption capacity of Ce-ZnO@HNTs upon loading of RES (Fig. 1(o)). In summary, compared to ZnO's nearly full wavelength shielding effect alone, CZHR exhibits a specific UV band of light. These structural and property advantages of Ce-ZnO@HNTs suggest that CZHR sunscreen emulsion will have a good UV resistance effect.

3.2 Formation and stabilization of CZHR Pickering emulsions

Unlike traditional emulsions stabilized by surfactants, HNTs adsorb at the oil-water interface, forming a tightly packed shell that encapsulates the oil phase, i.e., Pickering emulsion [35]. The wettability of solid particles at the oil-water interface determines their ability to adsorb and remain at the interface of droplets [36]. Hydrophilic particles can stabilize oil-in-water emulsions, whereas hydrophobic particles can stabilize water-in-oil emulsions. However, strongly hydrophilic/hydrophobic particles could not act as emulsion stabilizers, but they could remain in the aqueous/oil phase. Since raw HNTs is highly hydrophilic material with a water contact angle of ~ 10°, we utilized HDTMS to modify HNTs. The wettability of HNTs can be finely regulated through condensation reaction time (Fig. 2(a)). Figure 2(b) shows that the water contact angle of unmodified HNTs is 10.2° ± 2.6°, which increases to 34.0° ± 2.7° after reacting with HDTMS for 1 h, and reaches 69.5° ± 4.3° after 2 h of reaction.

Subsequently, Pickering emulsions based on Ce-ZnO@HNTs were prepared using liquid paraffin as the oil phase. Digital photographs and polarized optical microscopy (POM) images revealed that emulsions at different concentrations prepared with raw HNTs exhibited demulsification on the fifth day (Fig. S9 in the ESM). In contrast, the HDTMS-modified HNTs yielded stable Pickering emulsions with a uniform particle size distribution. These emulsions maintained their size and demonstrated excellent stability even after 30 days of storage. Therefore, the same method was applied to surface modification of Ce-ZnO@HNTs. To enhance the spreadability and film-forming properties of the sunscreen emulsions, PVA was incorporated to introduce a polymeric network structure, and the resulting Pickering emulsion sunscreen was named CZHR emulsion.

The POM images and particle size distribution result revealed a relatively uniform emulsion particle size, with an average oil droplet size of 7.8 μm (Figs. 2(c) and 2(d)). Rheological testing of the HNTs, Ce-ZnO@HNTs, and CZHR sunscreen emulsions showed shear-thinning or thixotropic behavior (Fig. 2(e)). This characteristic facilitates easy extrusion of the sunscreen from tube packaging while maintaining high stability under static conditions, thereby effectively preventing leakage. Furthermore, the critical role of CZHR in emulsion stabilization and formation was confirmed by fluorescence microscopy images, which showed FITC-labelled CZHR (green) surrounding Nile Red-stained oil droplets (red) (Fig. 2(f)).

To further evaluate the interfacial stability of CZHR, a Pickering emulsion was prepared using solid paraffin as the oil phase via an analogous method. Spherical oil droplets encapsulated by a dense layer of tubular nanostructures can be observed by SEM, further confirming the colloidal stability of CZHR (Fig. 2(g)). The sunscreen application process is illustrated in Fig. 2(h). Figure 2(i) confirms that the HNTs-based sunscreens exhibited comparable spreadability and skin adaptability to the commercial ANESSA sunscreen. Consequently, the Pickering emulsion stabilized by CZHR effectively resists phase separation, stratification, and emulsion breakdown, ensuring long-term storage stability.

3.3 UV protection and radiative cooling efficacy of CZHR sunscreen

To evaluate the *in vitro* efficacy of CZHR sunscreen in protecting against UV and inhibiting UV-induced ROS generation, a commercial sunscreen served as a positive control. UV transmittance was measured for all samples (Fig. S10 in the ESM). While the HNTs emulsion blocked ~ 76.5% of UV radiation, Ce-ZnO@HNTs, commercial sunscreen, and CZHR sunscreen demonstrated superior blocking efficiency, absorbing/scattering > 90% of UV radiation with specific rates of 91.7%, 93.2%, and 93.7%, respectively.

Furthermore, SPF values, a measure of UV protection efficacy, were 27.2 ± 3.6 and 53.2 ± 14.3 for the HNTs emulsion and Ce-ZnO@HNTs, respectively, demonstrating excellent UV protection (Fig. 3(a)). Further analysis of UVA and UVB transmittance indicated that HNTs emulsion effectively blocked the majority of UVB radiation, while Ce-ZnO@HNTs, commercial sunscreen, and CZHR sunscreen nearly achieved complete UVB blocking (Fig. 3(b)). Notably, the UV shielding performance of CZHR sunscreen surpasses that of Ce-ZnO@HNTs, which is attributed to the addition of the natural UV absorber RES.

ROS levels in UV-irradiated samples were measured using DHR,

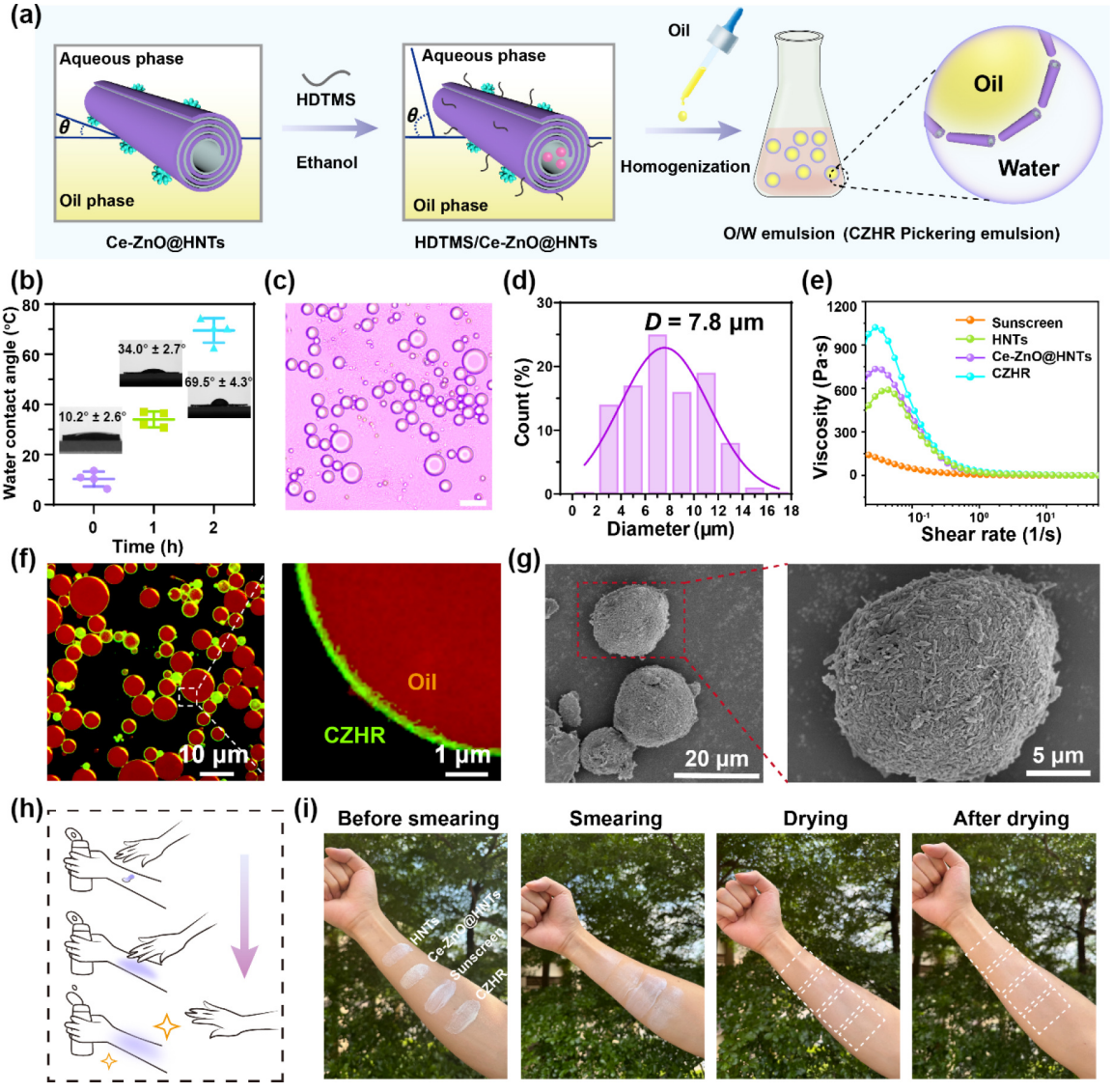

Figure 2 Preparation and characterization of CZHR Pickering emulsion. (a) Schematic diagram of CZHR Pickering emulsion preparation. (b) Contact angle of HDTMS-modified CZHR at different times. The data are presented as the mean ± SD, n = 3. (c) POM image of the CZHR Pickering emulsion after silane modification and (d) the corresponding particle size distribution. Scale bar: 20 μm. (e) Rheological testing of the apparent viscosity of commercial sunscreen, HNTs Pickering emulsion, Ce-ZnO@HNTs Pickering emulsion, and CZHR Pickering emulsion. (f) Fluorescence microscope images of CZHR Pickering emulsion. (g) SEM image. (h) Schematic diagram of CZHR Pickering emulsion application. (i) Photograph of emulsion application on human skin.

a common ROS detection probe [37]. The control (without sunscreen) showed increased fluorescence under UV irradiation. However, due to the UV-blocking effect of the sunscreens, the ROS signal detected does not increase over time in other protected groups (Fig. S11 in the ESM). At the 10-min point, the fluorescence signal of DHR in the unprotected group was 3.93-fold compared with the initial value, while the HNTs, Ce-ZnO@HNTs, commercial sunscreen, and CZHR emulsion protection groups were 1.70, 1.40, 1.39, and 1.26-fold, respectively (Fig. 3(c)). Therefore, the HNTs-based Pickering emulsion demonstrated excellent UV protection performance overall.

Subsequently, the solar spectral reflectance and mid-infrared emissivity of the CZHR sunscreen were evaluated. The CZHR emulsion exhibited high solar reflectivity (~ 0.73), while the HNTs emulsion showed slightly lower solar reflectance (~ 0.62) but remained higher than commercial sunscreen (~ 0.27) (Fig. 3(d)). According to Mie scattering theory, strong scattering occurs when the micro- and nanoscale dimensions of a material match the wavelengths of the solar spectrum (0.25 to 2.5 μm) [38]. The bright white appearance of HNTs makes them effective light scatterers. Based on these, CZHR was designed with particle sizes ranging from 0.3 to 2.0 μm, forming Pickering emulsion microspheres with a size distribution of 2–16 μm, which covers the entire solar spectrum and leads to broadband solar scattering. Furthermore, HNTs possess abundant molecular vibration peaks (Si–O, Si–O–Si and Al–O) in the mid-infrared band, which induces high mid-infrared emissivity (~ 0.87), endowing the Pickering emulsion with radiative self-cooling capabilities (Fig. 3(e)).

To preliminarily assess the solar reflection and thermal management capabilities of CZHR emulsion, a copper (Cu) plate was irradiated with simulated sunlight (1 sun), while infrared images were simultaneously captured using an IR camera (Figs. 3(f)–3(h)). Within 16 min, the temperature of the Cu plate coated with CZHR emulsion only rose from 28 to 43.0 °C, which

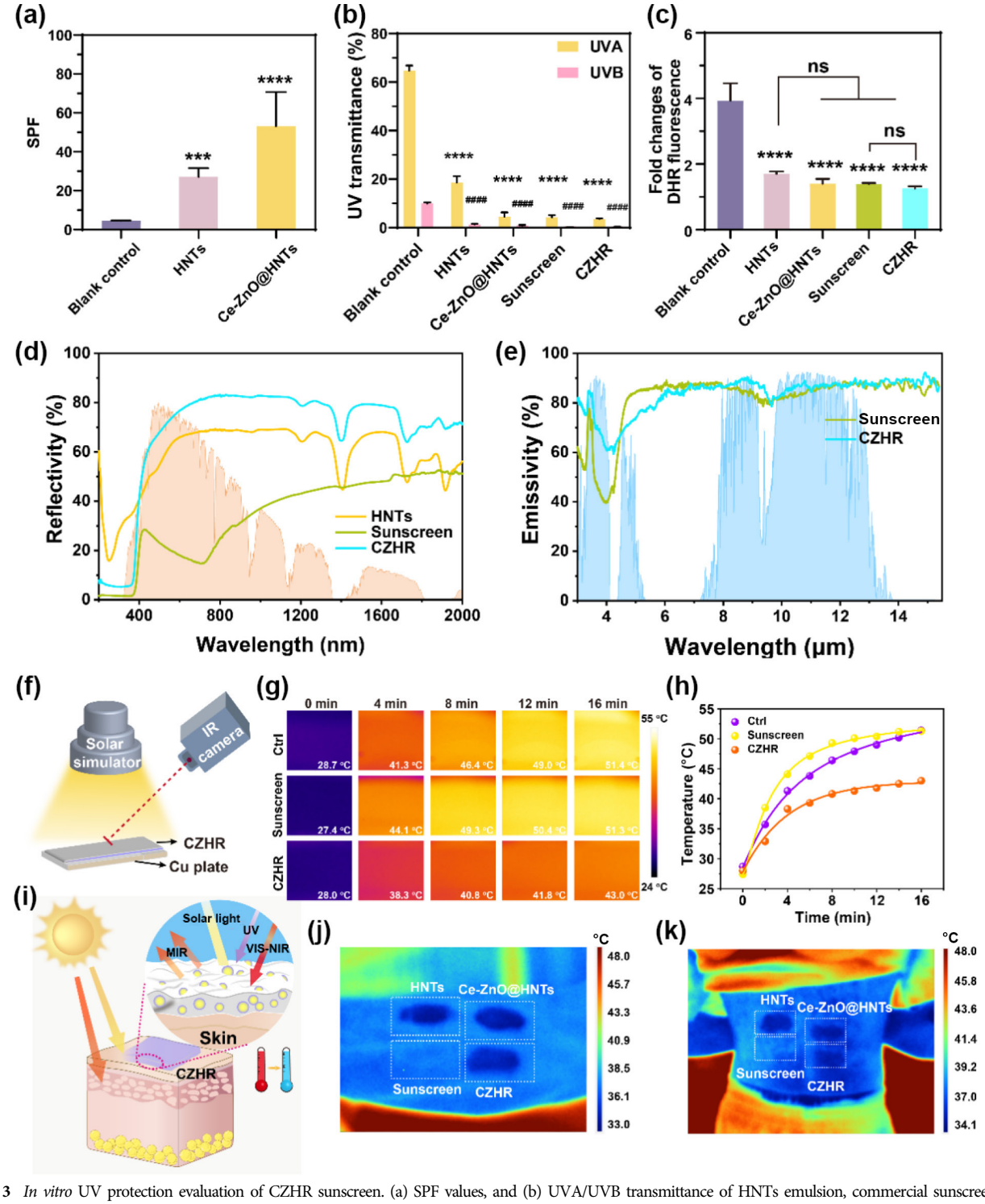

Figure 3 *In vitro* UV protection evaluation of CZHR sunscreen. (a) SPF values, and (b) UVA/UVB transmittance of HNTs emulsion, commercial sunscreens, and CZHR sunscreen. (c) The fold changes of the fluorescence of DHR at the 10 min post UV exposure. (d) Solar reflectivity of the CZHR sunscreen. (e) MIR emissivity of the CZHR sunscreen and commercial sunscreen products. (f) Schematic diagram of simulated solar heating test. (g) Infrared thermal images of the copper sheet under simulated sunlight. (h) Temperature change curve. (i) Schematic of the radiative thermal management regulation principle of CZHR sunscreen. (j) Infrared thermal image of covering different sunscreens on the human arm in a sunny outdoor environment. (k) Infrared thermal image of covering different sunscreens on the human back in a sunny outdoor environment.

was significantly lower than the control (51.4 °C) and the Cu plate coated with commercial sunscreen (51.3 °C). This demonstrates the strong radiative cooling effect of the prepared CZHR sunscreen.

Furthermore, to evaluate the real-world cooling efficacy of CZHR sunscreen, we performed *in-situ* temperature measurements on human skin. Guangzhou (113°15'53" E, 23°06'32" N) was chosen as the experimental location due to its representative hot outdoor climate, mirroring a typical application environment for sunscreens. Figure 3(i) illustrates the principle by which the CZHR sunscreen regulates human skin temperature. Commercial

sunscreens, while incorporating inorganic UV blockers like ZnO and TiO_2, also contain organic UV absorbers. These absorbers convert a portion of the absorbed UV energy into thermal energy, leading to a skin temperature under the sunscreen that is comparable to that of exposed skin. In contrast, the HNTs-based sunscreen exhibited substantial cooling capabilities on the arm. Specifically, the skin temperatures in areas protected by HNTs, Ce-ZnO@HNTs, and CZHR sunscreens were reduced by 2.3, 1.8, and 1.7 °C, respectively, compared to both the exposed skin area and the area covered by commercial sunscreen (Fig. 3(j) and Fig. S12(a) in the ESM). Similar exceptional cooling performance was observed in the back test area with CZHR sunscreen, where temperatures were 3.1 and 2.9 °C lower than the exposed skin and commercial sunscreen-covered areas, respectively (Fig. 3(k) and Fig. S12(b) in the ESM). Consequently, the CZHR sunscreen can establish an ideal thermal environment for the skin in sunlight, leading to an improved experience for outdoor workers.

3.4 CZHR sunscreen for keratinocyte protection from UV-induced photodamage

The UV protection effect of CZHR sunscreen *in vitro* was evaluated using the keratinocyte cell line HaCaT as a model (Fig. 4(a)). Firstly, the cytotoxicity of CZHR was evaluated using an MTT assay. The results showed that the cell viability of CZHR group with different concentrations for 24 h was > 90%, indicating good biocompatibility (Fig. S13 in the ESM). To simulate sunscreen application to the skin, HaCaT cells were covered with optical quartz slides pre-coated with a thin layer of test sunscreen and then exposed to UV radiation. MTT assays revealed that HaCaT cell viability was significantly reduced to 71.3% ± 8.5% after UV radiation (Fig. 4(b)). In contrast, cell viability in the commercial sunscreen, Ce-ZnO@HNTs, and CZHR groups remained above 90%, which was comparable to the normal group. The live/dead staining results were consistent with the MTT assay (Fig. 4(c) and Fig. S14 in the ESM). Upon exposure of HaCaT to UV, a significant increase in fluorescence intensity (red) indicative of high cell death levels was observed. Notably, fluorescence images demonstrated that treatment with different sunscreens can efficiently support HaCaT cell survival, as evidenced by a marked attenuation of the red fluorescence signals.

UV radiation damages DNA by inducing covalent cross-links between adjacent pyrimidines, forming pyrimidine dimers that distort the DNA structure, which can result in replication errors, genome instability, and ultimately cancer [39]. As a response to DNA damage, H2AX is phosphorylated at the serine residue number 139 (known as γH2AX) [40]. As illustrated in Fig. 4(d) and Fig. S15 in the ESM, treatment with HNTs reduced the proportion of γ-H2AX-positive cells. Furthermore, Ce-ZnO@HNTs, commercial sunscreen, and CZHR sunscreen significantly attenuated the formation of γ-H2AX-positive foci in keratinocytes, attributable to their high-efficiency UV-blocking capabilities.

The proportion of apoptotic cells after UV irradiation was quantified using Annexin V/PI flow cytometry. Compared to the unprotected group (18.8%), the HNTs, Ce-ZnO@HNTs, commercial sunscreen, and CZHR sunscreen groups exhibited significantly lower apoptosis rates (Fig. 4(e)). Furthermore, UV-induced DNA damage and apoptosis can impair normal cellular functions, such as cell migration. The scratch assay suggested that the migration speed of HaCaT cells was reduced after UV irradiation, but the migration speed in the groups with different treatments significantly increased, approaching the levels of normal cells (Fig. 4(f) and Fig. S16 in the ESM). So, sunscreen formulations based on Ce-ZnO@HNTs effectively inhibit UV-induced DNA damage and apoptosis in skin cells, thereby reducing the risks of mutations and malignant transformation.

3.5 *In vitro* antibacterial properties and biofilm inhibition of Ce-ZnO@HNTs

In skin infections, bacteria typically adhere firmly to the skin surface by secreting substances like polysaccharides, and then gradually aggregate to form biofilms [41]. Biofilm formation significantly hinders drug penetration and enhances bacterial resistance, posing a persistent and serious problem in skin infections [42]. Excessive accumulation of ROS is widely recognized for its ability to disturb various physiological responses in bacteria, leading to redox imbalances and oxidative stress damage [43].

Antimicrobial activity of Ce-ZnO@HNTs against planktonic *S. aureus* and *E. coli* was first evaluated using colony counting. As shown in Fig. 5(a), HNTs treatment showed no significant impact compared to PBS. Conversely, Ce-ZnO and Ce-ZnO@HNTs significantly reduced *S. aureus* viability to 9.6% and 7.1%, and *E. coli* viability to 18.4% and 18.7%, respectively (Figs. 5(c) and 5(d)). Under UV irradiation, Ce-ZnO and Ce-ZnO@HNTs groups eliminated over 97.4% and 99.7% of *S. aureus*, and 89.8% and 93.1% of *E. coli*, respectively. This suggests that Ce-ZnO exhibits enhanced antibacterial activity under UV irradiation, attributed to the elevated generation of ROS resulting from improved photoelectron transfer and separation, while HNTs aid in the dispersion of Ce-ZnO nanoparticles, further improving antibacterial efficacy.

The anti-biofilm formation activity of Ce-ZnO@HNTs was further evaluated *in vitro* using the crystal violet staining method. As shown in Fig. 5(b), biofilms treated with PBS and UV irradiation maintained their vitality and structural integrity, indicating that UV exposure is biologically safe. After co-culturing with Ce-ZnO (UV−) and Ce-ZnO@HNTs (UV−), a significant reduction in staining intensity and biofilm biomass was observed. The Ce-ZnO@HNTs (UV+) group showed markedly increased biofilm disruption, with nearly no intact biofilm remaining. Quantitative analysis of the biofilms yielded consistent results (Figs. 5(e) and 5(f)). The inhibitory effect of Ce-ZnO@HNTs on biofilm was found to be concentration-dependent regardless of UV irradiation (Fig. S17 in the ESM). The antibiofilm formation result is consistent with the colony counting result above.

Furthermore, SEM images revealed dense and intact biofilms formed in both control and UV groups (Fig. 5(g) and Fig. S18 in the ESM). Numerous bacteria with complete structures were embedded within an extracellular polymer substance matrix, forming stacked colonies. In contrast, the extracellular polymer matrix in the Ce-ZnO@HNTs treated group was almost invisible, with only sporadic microcolonies observed. Bacteria lacking biofilm protection were exposed, showing evident structural damage at the interface with Ce-ZnO@HNTs (Figs. 5(h) and 5(i)). This damage included distortion of bacterial shape, surface wrinkling, and even rupture. It suggests that the sharp nanotube structures can physically damage bacteria through penetration, compromising their structural integrity, and disrupting membrane stability and homeostasis. Under the synergistic effect of UV irradiation, the release of numerous bacterial membrane vesicles indicates that UV absorption by Ce-ZnO@HNTs more strongly affects bacterial membrane homeostasis, triggering blistering of the outer

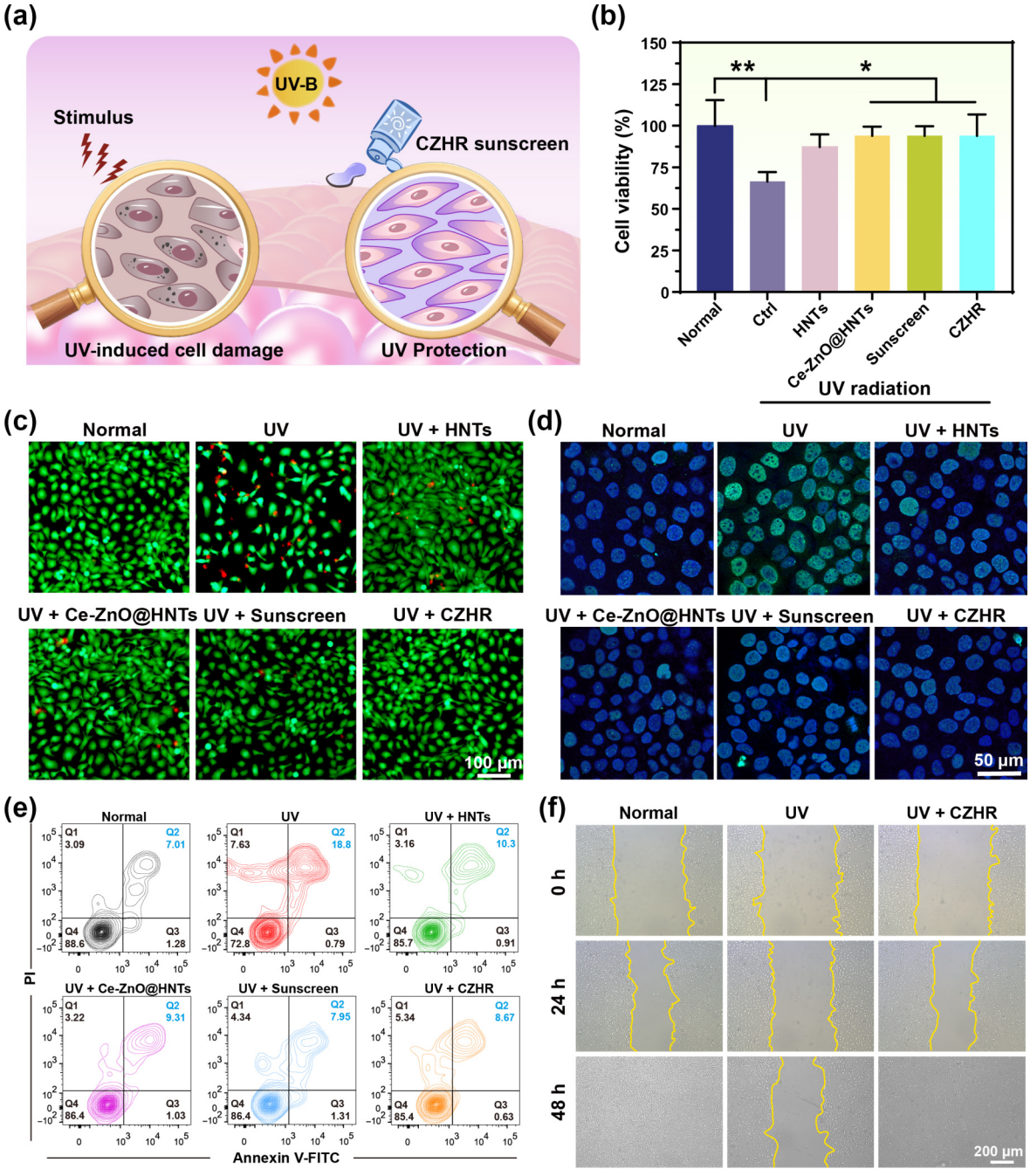

Figure 4 CZHR sunscreen for keratinocyte protection from UV-induced photodamage. (a) Schematic description of keratinocyte protection by CZHR sunscreen against UV irradiation. (b) Cell viability and (c) calcein AM/PI live/dead staining of HaCaT cells after different treatments. (d) Immunofluorescence images of γH2AX. (e) The representative flow cytometric analysis of Annexin V/PI of HaCaT cells after 6 h of UV irradiation. (f) The scratch images of the UV-induced photodamaged HaCaT cells at 0, 24, and 48 h after being treated with CZHR sunscreen. Scale bar: 200 μm. The data are presented as the mean ± SD, $n = 3$. P values were assessed by one-way ANOVA with Tukey's post-hoc test. $^*P < 0.05$, $^{**}P < 0.01$.

membrane and vesicle release, which ultimately results in bacterial death. Live/dead staining showed a significant reduction in both fluorescence intensity and biofilm thickness in the treatment groups of Ce-ZnO and Ce-ZnO@HNTs (Fig. 5(j)). Comprehensive analysis indicated that, following UV absorption, Ce-ZnO@HNTs exhibited superior biofilm formation inhibition capabilities compared to Ce-ZnO.

Ce-ZnO@HNTs exhibits broad-spectrum antibacterial properties and enhanced biofilm inhibition, attributable to the synergistic action of interfacial interactions, physical penetration, Zn^{2+} release, and oxidative stress (Fig. 5(k)). Mechanical penetration is generally regarded as the primary way high-aspect-ratio nanoparticles act on the adhered bacteria [44]. This process leads to the rupture of bacterial membranes and leakage of intracellular proteins. Ce-ZnO synthesised on HNTs can directly contact bacteria and disrupt their membrane integrity via electrostatic adsorption. The antibacterial activity of Ce-ZnO@HNTs is primarily due to the generation of highly active ROS that damage and kill bacteria [45]. These ROS, such as hydroxyl (·OH) and superoxide ($\cdot O_2^-$) radicals, attack and destroy bacterial cell

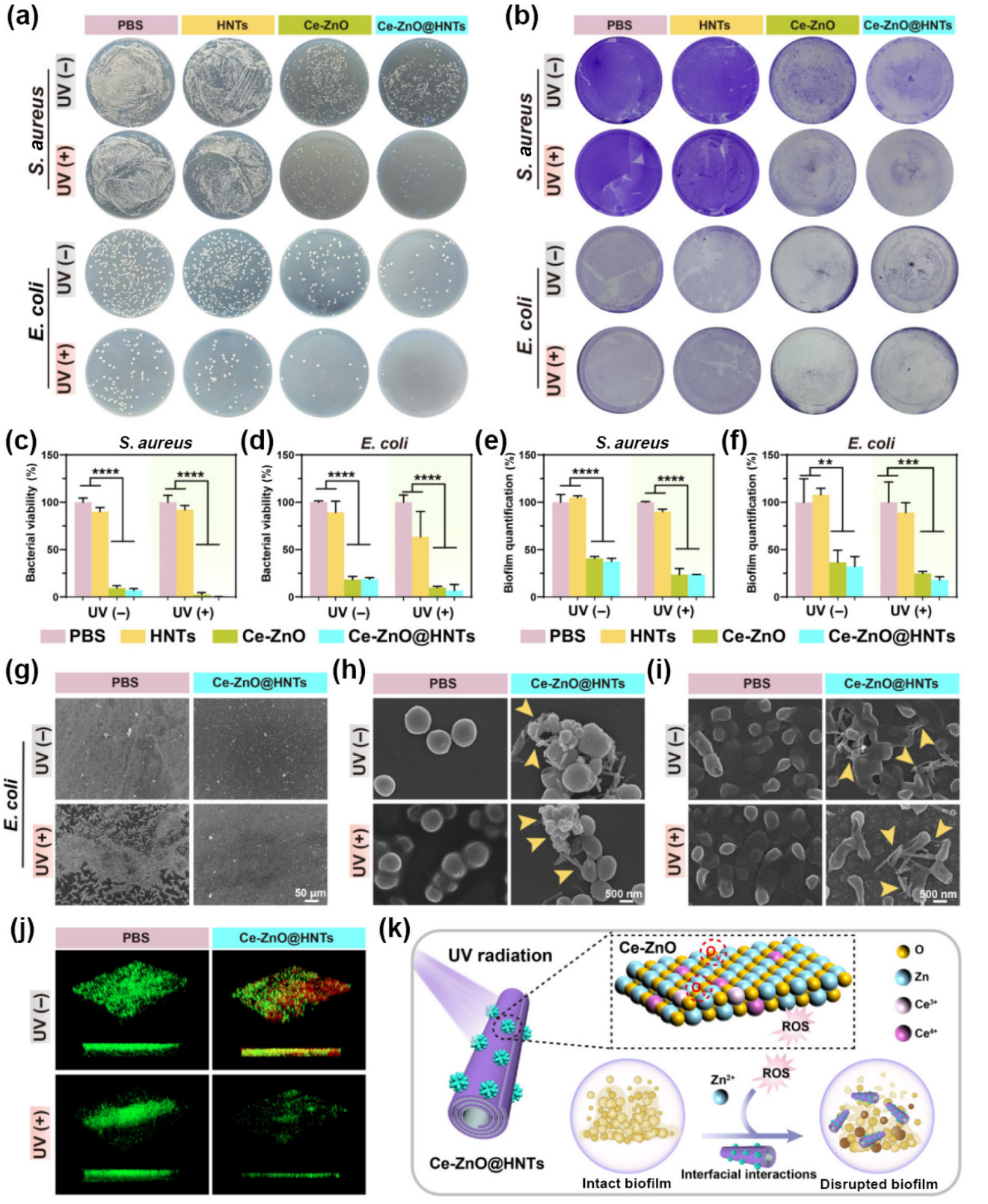

Figure 5 *In vitro* antibacterial and antibiofilm properties of Ce-ZnO@HNTs. (a) Representative agar plate photographs. (b) Crystal violet staining assay of *S. aureus* and *E. coli* biofilms after different treatments. Bacterial viability of (c) *S. aureus* and (d) *E. coli* after different treatments, including PBS, HNTs, Ce-ZnO, and Ce-ZnO@HNTs. UV (–/+) stands for the UV lamp off and on, respectively. The corresponding quantitative statistics of (e) *S. aureus* and (f) *E. coli* biofilm crystal violet staining. (g) Representative SEM images of *E. coli* biofilms 24 h after different treatments. (h, i) Representative SEM images showing the microscopic morphology of bacterial membranes 36 h after Ce-ZnO@HNTs treatment with UV (–/+). (j) Representative 3D images of *S. aureus* biofilms after Ce-ZnO@HNTs treatment with UV (–/+). Data are represented as mean ± SD. (k) Schematic diagram of the CZHR antibacterial mechanism. Data are presented as mean ± SD, $n = 3$. P values were assessed by one-way ANOVA with Tukey's post-hoc test. $^{**}P < 0.01$, $^{***}P < 0.001$, $^{****}P < 0.0001$.

membranes, proteins, and DNA, leading to bacterial inactivation and death [46]. The Ce dopant in Ce-ZnO@HNTs promotes the accumulation of ROS generated from photogenerated holes upon UV absorption [25]. It is noteworthy that the effective dispersion of Ce-ZnO on HNTs is crucial for its excellent antibacterial efficacy, even at low concentrations.

3.6 Evaluation of the skin penetration and adhesion properties

Ideally, an effective sunscreen should remain on the skin's surface to minimize potential health risks associated with cutaneous absorption (Fig. 6(a)). To investigate skin retention and penetration, both ZnO and CZHR nanoparticles were labelled with FITC. Following topical application to murine skin and a 6-h incubation period, the penetration of each group was assessed via fluorescence imaging. As indicated in Fig. 6(b), the CZHR predominantly remained on the skin surface, evidenced by a robust green fluorescence signal. In contrast, the ZnO group displayed significantly weaker fluorescence signals, indicating that CZHR exhibited substantially greater skin retention compared to ZnO. The prolonged skin retention of CZHR is likely attributable to the tubular morphology of HNTs, which provides a larger surface area and increased adsorption sites, thereby enhancing physical contact with the skin. Importantly, no evidence of CZHR nanoparticle penetration was observed within the histological sections of skin samples, eliminating the potential for epidermal, dermal, or follicular translocation. This observation effectively mitigates concerns regarding skin safety related to nanoparticle penetration and systemic absorption.

Subsequently, FITC-labelled CZHR sunscreen was topically applied to the mice's skin to assess its retention. Fluorescence signals at various time points were monitored and quantified using a small animal IVIS (Figs. 6(c) and 6(e)). The results showed that the fluorescence intensity on the skin did not change significantly, even after 6 h, indicating that the sunscreen could remain on the skin. In addition, the water resistance and mechanical removal properties of the CZHR sunscreen were further investigated. The results (Figs. 6(d) and 6(g)) showed that the fluorescence intensity of the CZHR sunscreen changed only slightly after rinsing with running water, suggesting good water resistance of the formulation. This is attributable to the incorporation of PVA, which facilitates the formation of a stable film on the skin surface [47]. Nevertheless, gentle wiping with a wet towel resulted in a rapid decrease in fluorescent signal (Fig. 6(f)), indicating that, despite its water resistance, the sunscreen is susceptible to removal via mechanical forces. Unlike commercial sunscreens, which contain multiple chemical additives to promote film formation and stabilization, formulations based on HNTs reduce the risk of irritation and allergic contact dermatitis.

The skin safety of the samples was studied by applying PBS, HNTs emulsion, Ce-ZnO@HNTs sunscreen, commercial sunscreen, and CZHR sunscreen to the dorsal of mice for seven consecutive days. Cross-sections of the skin were then taken for H&E staining. The results showed no significant differences between the treatment and PBS control groups. No pathological changes, such as keratin thickening, inflammatory cell infiltration, or structural abnormalities, were observed in any samples (Fig. 6(h)). No abnormalities were found in the H&E staining of pathological sections of major organs, nor the complete blood routine tests (Figs. S19 and S20 in the ESM). In total, CZHR demonstrates a high safety profile, laying the foundation for further development and application.

3.7 *In vivo* UV protection efficiency

UV radiation can directly damage DNA in skin tissues, disrupting the redox balance and increasing levels of inflammatory mediators. This leads to cellular dysfunction and the potential for malignant transformation [48]. The protective effects of CZHR sunscreen against UV radiation were studied using high doses of UVB radiation (Fig. 7(a)). The designated UV-exposure area on the back of each mouse was divided into six quadrants. Each quadrant was treated with one of the following: saline (positive control), HNTs emulsion, Ce-ZnO@HNTs sunscreen, commercial sunscreen, or CZHR sunscreen. The remaining area was covered with sterilized black fabric, serving as a healthy control.

Following three 15-min UV exposures, representative photographs of the skin from different groups were captured (Fig. S21 in the ESM). Initially, the skin of mice in the control group appeared smooth and flat, with no discernible erythema or wrinkles. After UV exposure, the UV group exhibited signs of damage, including rough and peeling skin. However, the skin of mice in the Ce-ZnO@HNTs, Sunscreen, and CZHR protection groups did not differ significantly from the control group. The mice's skin tissues were then collected for histological analysis. H&E staining revealed that the epidermal layer of the UV group was 6.82-fold thicker than that of the healthy control group, measuring 118.66 ± 21.93 μm (Fig. 7(b)). This increase was accompanied by pronounced acanthosis and epidermal hyperplasia. Previous studies have shown that epidermal hyperplasia may be due to increased keratinocyte differentiation induced by UV irradiation or mitochondria-derived ROS [46, 49]. Conversely, epidermal thickness increased to a lesser extent in other UV-exposure groups. The epidermal thickness was measured as 60.64 ± 19.00 μm in the HNTs emulsion group, 36.86 ± 8.85 μm in the Ce-ZnO@HNTs sunscreen group, 31.46 ± 4.73 μm in the commercial sunscreen group, and 28.86 ± 5.48 μm in the CZHR sunscreen group (Fig. 7(e)). This suggests that the Ce-ZnO@HNTs sunscreen did not induce the epidermal thickness increase after UV-exposure.

Masson's trichrome staining revealed a significant 293% increase in keratin expression in unprotected skin compared to the healthy control (Figs. 7(c) and 7(f)). This increase represents a hallmark response of skin tissue to UV damage, which can lead to hyperkeratosis and potentially keratosis pilaris, a condition characterized by follicular bumps, blockage of the follicular opening, and subsequent inflammation [50]. Conversely, keratin expression was significantly reduced in all UV-protected groups. Furthermore, toluidine blue staining of the Ce-ZnO@HNTs and CZHR groups demonstrated minimal mast cell infiltration (Fig. 7(d)), comparable to the healthy control. Given that mast cells are implicated in the production of inflammatory cytokines, an increase in their number is indicative of inflammation (Fig. 7(g)). These findings suggest that sunscreen products formulated with Ce-ZnO@HNTs effectively mitigate UV-induced skin pathology.

Skin exposure to UV radiation induces intracellular oxidative stress, leading to an abnormal accumulation of ROS and, in turn, oxidative DNA damage [51]. 8-hydroxydeoxyguanosine (8-OHdG) is a marker of oxidative DNA damage, commonly used as an indicator to assess the extent of oxidative skin damage [52]. In a UV-induced mouse skin damage model, the expression of 8-OHdG was elevated (Fig. 8(a)). Following treatment with HNTs emulsion, Ce-ZnO@HNTs sunscreen, commercial sunscreen, and CZHR sunscreen, the levels of 8-OHdG decreased by 34.66%, 44.09%, 38.97%, and 42.70%, respectively, suggesting that CZHR is effective in preventing UV-induced oxidative DNA damage (Fig. 8(d)).

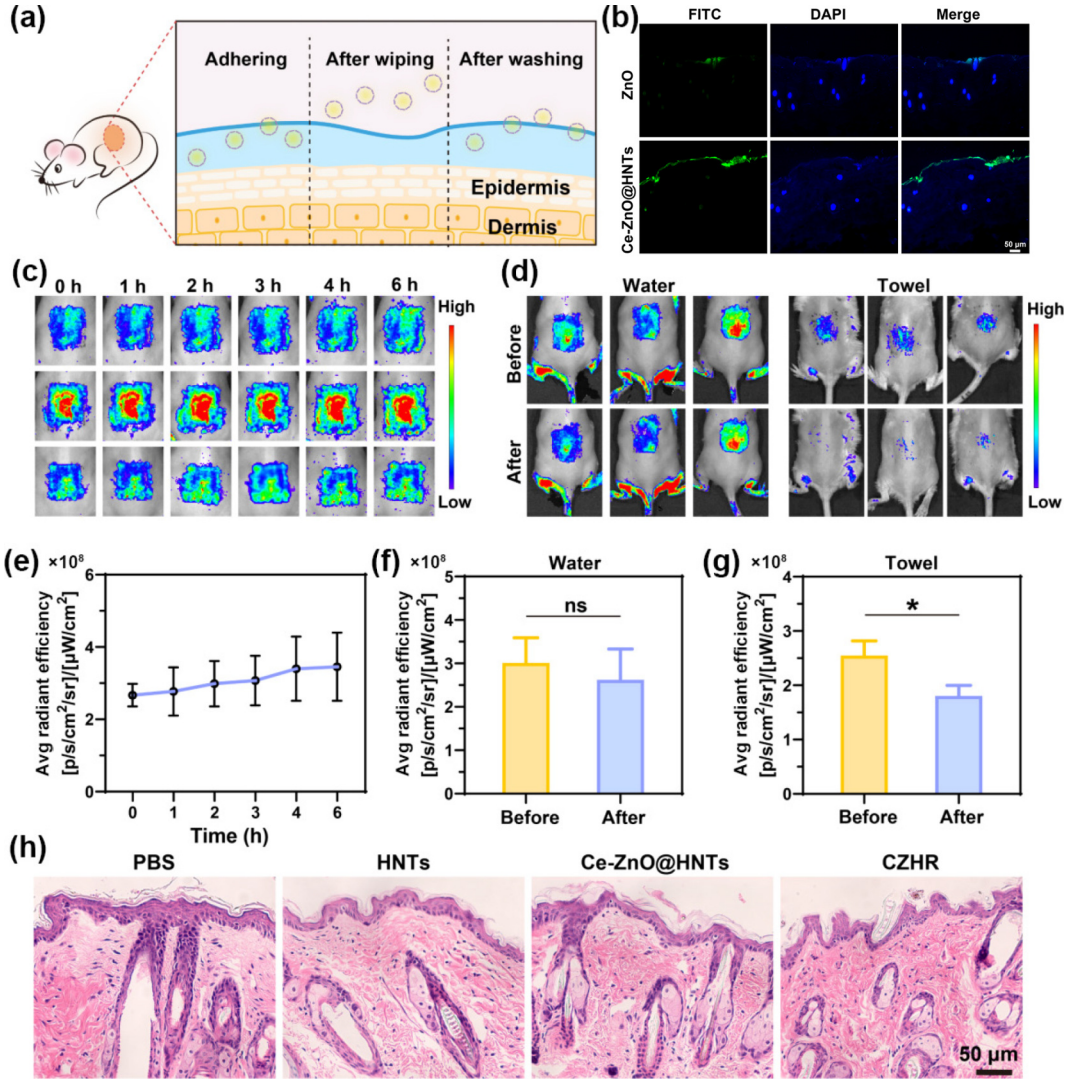

Figure 6 *In vivo* skin penetration and safety evaluation of CZHR. (a) Schematic diagram of *in vivo* skin penetration of CZHR emulsion. (b) Skin penetration of ZnO and CZHR nanoparticles. The particles were incubated on the dorsal side of mice for 6 h. (c) IVIS images of CZHR emulsion retention on the dorsal side of mice at different time points. (d) IVIS images of CZHR emulsion retention after washing with water or wiping with a wet towel. (e) Quantitative analysis of emulsion retention at different time points. Quantitative analysis of emulsion retention after (f) washing and (g) wiping. (h) H&E staining images of skin sections. The data are presented as the mean ± SD, $n = 3$.

Previous studies have shown that abnormally activated ROS react with DNA in cells, leading to double-strand breaks, and subsequently promoting the formation of γH2AX [53–55]. Sustained γH2AX expression can result in genomic instability and increase the risk of cellular carcinogenesis. Unprotected mice exhibited the most pronounced recruitment of γH2AX, indicating the highest level of DNA damage, particularly in the basal layer of the epidermis (Fig. 8(b)). Treatment with HNTs emulsion, Ce-ZnO@HNTs, and commercial sunscreen resulted in significant reductions in γH2AX expression, decreasing by 33.19%, 49.66%, and 48.50%, respectively, compared to the unprotected group (Fig. 8(e)). Notably, the γH2AX level in the CZHR group was comparable to that of the healthy control group, with a 57.66% reduction. Furthermore, immunohistochemical results revealed a reduced expression level of IgE, suggesting that Ce-ZnO@HNTs may inhibit the production of IgE-related immune factors, thereby alleviating the immune response and reducing inflammation (Fig. 8(c)).

After UV irradiation, the repair effects of different treatments were evaluated (Fig. S22 in the ESM). The untreated group exhibited severe skin damage, including ulceration, erythema, and exudation, whereas the CZHR group showed extensive skin recovery and hair regrowth. These findings were corroborated by H&E staining results (Fig. S23 in the ESM). The CZHR group demonstrated the most favorable overall performance in terms of both skin protection and repair, likely due to the sustained release of resveratrol from CZHR, which counteracted or mitigated the adverse reactions induced by UV radiation. Overall, CZHR sunscreen can effectively prevent UV-induced epidermal hyperplasia, keratin thickening, oxidative cellular damage, base mutations, abnormal cellular function, an inflammatory response, and even malignant cellular transformation (Fig. 8(f)).

4 Conclusions

In summary, natural nanoclay HNTs was employed to develop a multifunctional emulsion for advanced skin management,

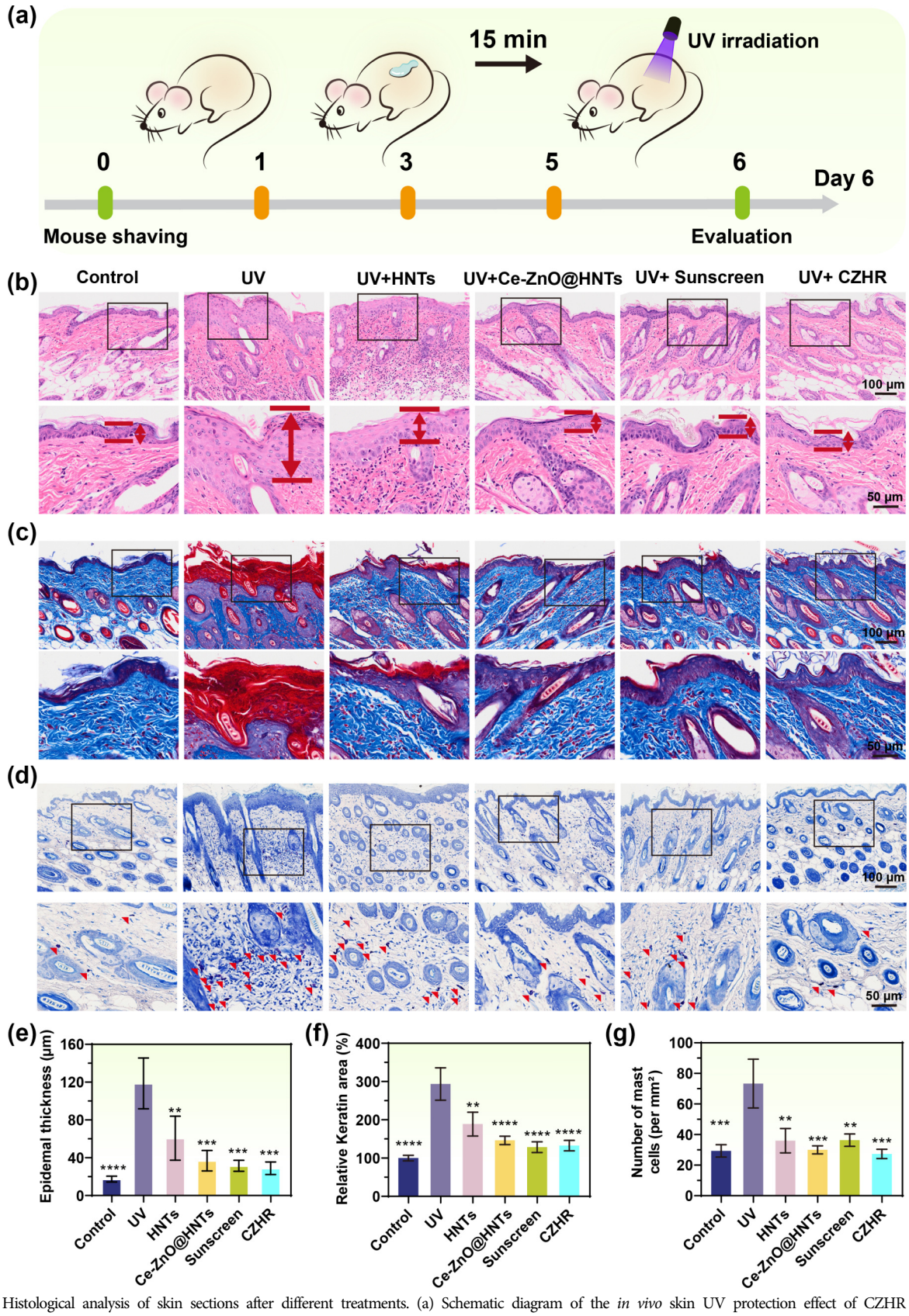

Figure 7 Histological analysis of skin sections after different treatments. (a) Schematic diagram of the *in vivo* skin UV protection effect of CZHR sunscreen. (b) Representative H&E staining images of skin sections. The red triangle denotes dermal mast cells. (c) Representative Masson's trichrome staining images of skin sections. (d) Representative toluidine blue staining of skin sections. (e) Measurement of skin epidermal thickness for each group after treatments. (f) The relative Keratin percentage of mice's dorsal skin sections after different treatments. (g) Measurement of the density of mast cells for each group after treatments. *P* values were assessed by one-way ANOVA with Tukey's post-hoc test. $^{**}P < 0.01$, $^{***}P < 0.001$, $^{****}P < 0.0001$.

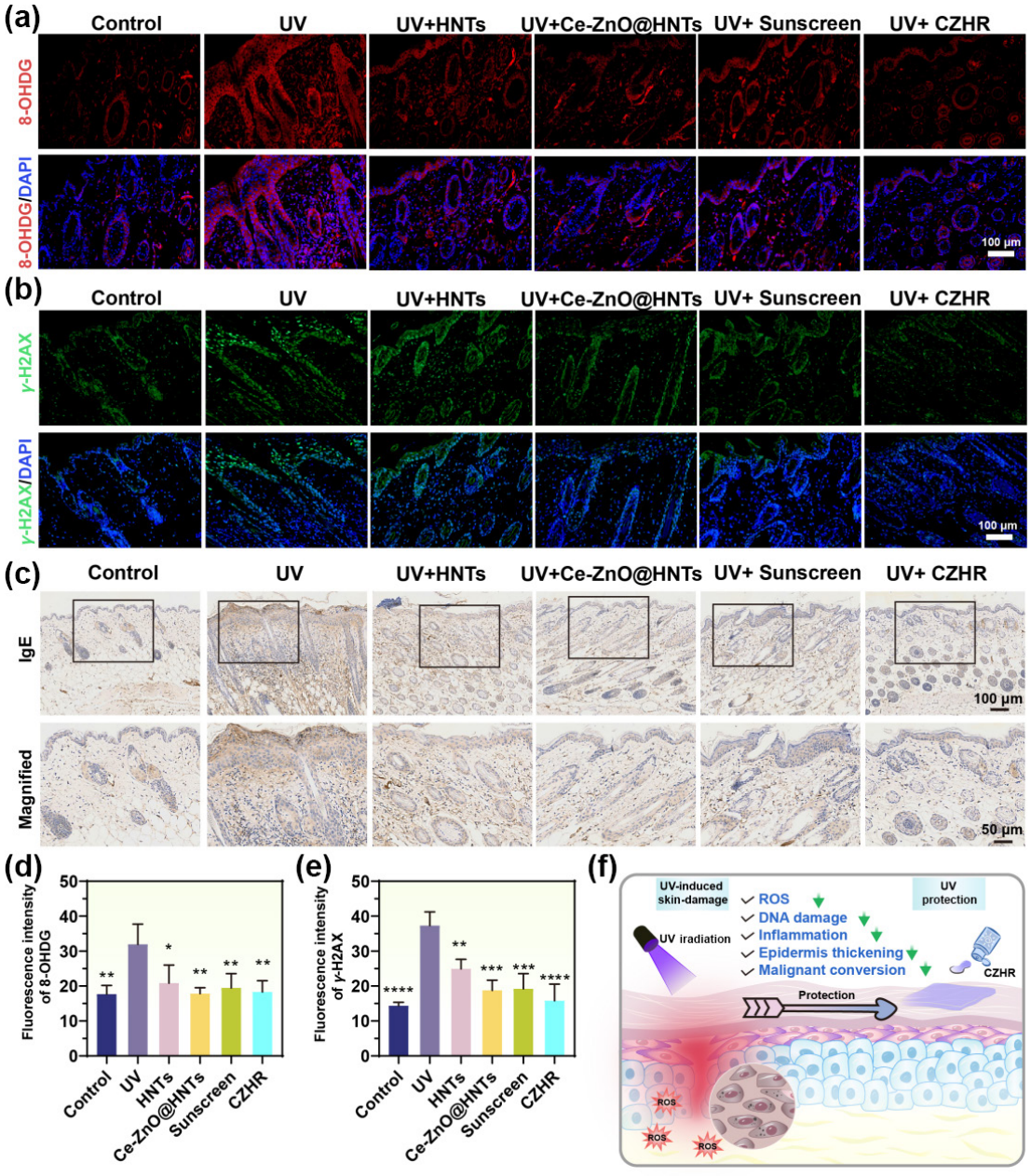

Figure 8 Evaluation of oxidative stress, inflammation, and epidermal barrier damage. (a) Immunofluorescence staining of 8-OHDG (red), and (b) γH2AX (green) on mice dorsal skin sections. Nuclei were stained with DAPI (blue). (c) Immunohistochemical staining of IgE. (d) Quantitative analysis of the levels of 8-OHDG, and (e) γH2AX. (f) Schematic diagram of the protective mechanism of CZHR sunscreen against UV damage in mice. *P* values were assessed by one-way ANOVA with Tukey's post-hoc test. $^{**}P < 0.01$, $^{***}P < 0.001$, $^{****}P < 0.0001$.

specifically addressing UV protection, radiative cooling, and biofilm inhibition. Specifically, the surface modification of HNTs by anchoring Ce-ZnO nanoparticles results in enhanced UV absorption performance. RES is loaded into HNTs to further enhance UV shielding and confer antioxidant protection. The CZHR effectively inhibits biofilm formation by disrupting bacterial cell membranes, thereby preventing bacterial colonization on the skin. The resulting CZHR Pickering emulsion demonstrates excellent UV protection and radiative cooling effects both *in vitro* and *in vivo*. Notably, HNTs serve as a critical nanoplatform for achieving the *in-situ* synthesis of Ce-ZnO, functioning as an interface stabilizer within Pickering emulsions, and imparting enhanced UV protection and radiation cooling properties to the formulation. This innovative approach combines *in-situ* synthesis of inorganic UV filters with the loading of natural polyphenol ingredients onto HNTs, which offers prospective insights into skin UV protection and outdoor thermal management.

Electronic Supplementary Material: Supplementary material (UV absorption curves; XRD patterns; SEM images; TEM images; particle size distribution of HNTs and Ce-ZnO@HNTs; XPS spectra; appearance and POM images of Pickering emulsion; UV transmittance rate and the corresponding photographs of the UV intensity indicator cards; the corresponding average temperature of skin simulators covered with different sunscreens; cytotoxicity, cell migration, biofilm inhibition, biosafety evaluation, and *in vivo* UV

protection study) is available in the online version of this article at https://doi.org/10.26599/NR.2026.94908443.

Data availability

All data needed to support the conclusions in the paper are presented in the manuscript and the Electronic Supplementary Material. Additional data related to this paper may be requested from the corresponding author upon request.

Acknowledgements

This work acknowledges the financial support received from the National Natural Science Foundation of China (No. 52573297), Natural Science Foundation of Guangdong Province (No. 2025A1515011860), and Fundamental Research Funds for the Central Universities (No. 21624115).

Declaration of competing interest

All the contributing authors report no conflict of interests in this work.

Author contribution statement

X. Y. C.: performed in conceptualization, data curation, formal analysis, investigation, methodology, writing – original draft. Y. W. Q.: performed in formal analysis, investigation. S. Q. Z.: performed in formal analysis, methodology. C. C. M.: performed in formal analysis, software. H. L.: performed in resources, and writing – review & editing. M. X. L.: performed in funding acquisition, project administration, resources, writing – review & editing, and supervision.

Informed consent

Not applicable.

Ethics statement

Female KM mice (6–8 weeks old) were housed at Guangdong Huawei Testing Co., Ltd. and operated on according to the protocols of its ethics committee, with free access to food and water throughout the study (Ethical code: 202408005).

Use of AI statement

None.

References

[1] Deng, Y.; Ediriwickrema, A.; Yang, F.; Lewis, J.; Girardi, M.; Saltzman, W. M. A sunblock based on bioadhesive nanoparticles. *Nat. Mater.* **2015**, *14*, 1278–1285.

[2] Eller, M. S.; Asarch, A.; Gilchrest, B. A. Photoprotection in human skin-a multifaceted SOS response. *Photochem. Photobiol.* **2008**, *84*, 339–349.

[3] Schneider, S.; Parsons, Z. A.; Leer, S. Beyond the scoreboard: Coaches' UV-related skin cancer knowledge in outdoor sports. *J. Eur. Acad. Dermatol. Venereol.* **2025**, *39*, 1297–1305.

[4] Wysong, A.; Gladstone, H.; Kim, D.; Lingala, B.; Copeland, J.; Tang, J. Y. Sunscreen use in NCAA collegiate athletes: Identifying targets for intervention and barriers to use. *Prev. Med.* **2012**, *55*, 493–496.

[5] Romanhole, R. C.; Ataide, J. A.; Moriel, P.; Mazzola, P. G. Update on ultraviolet A and B radiation generated by the sun and artificial lamps and their effects on skin. *Int. J. Cosmet. Sci.* **2015**, *37*, 366–370.

[6] Verma, A.; Zanoletti, A.; Kareem, K. Y.; Adelodun, B.; Kumar, P.; Ajibade, F. O.; Silva, L. F. O.; Phillips, A. J.; Kartheeswaran, T.; Bontempi, E. et al. Skin protection from solar ultraviolet radiation using natural compounds: A review. *Environ. Chem. Lett.* **2024**, *22*, 273–295.

[7] Yamada, M.; Mohammed, Y.; Prow, T. W. Advances and controversies in studying sunscreen delivery and toxicity. *Adv. Drug Deliv. Rev.* **2020**, *153*, 72–86.

[8] Xu, J. Q.; Wu, X. K.; Li, Y. R.; Zhao, S. M.; Lan, F.; Xi, A. K.; Huang, Y.; Ding, Y. L.; Zhang, R. F. High-performance radiative cooling sunscreen. *Nano Lett.* **2024**, *24*, 15178–15185.

[9] Kwon, J.; Kim, M.; Kim, Y. J.; Oh, H.; Lee, J. B.; Yi, G. R.; Lee, H. Titania-cored Janus multipods as UV-protective Pickering emulsifiers for sunscreens. *Small* **2025**, *21*, 2402577.

[10] Weng, Z. Z.; Wei, Q.; Ye, C.; Xu, Y. Y.; Gao, J.; Zhang, W.; Liu, L. B.; Zhang, Y.; Hu, J. N.; Zhong, Q. et al. Traditional herb (Moxa) modified zinc oxide nanosheets for quick, efficient and high tissue penetration therapy of fungal infection. *ACS Nano* **2024**, *18*, 5180–5195.

[11] Holmes, A. M.; Song, Z.; Moghimi, H. R.; Roberts, M. S. Relative penetration of zinc oxide and zinc ions into human skin after application of different zinc oxide formulations. *ACS Nano* **2016**, *10*, 1810–1819.

[12] Yang, Y. D.; Liu, X. Y.; Wan, C. C.; Liu, S. L.; Li, X. G.; Zhu, Y.; Yang, Z. X.; Li, L. L.; Zhang, Z.; Zhou, Z. Y. et al. Powering the future green buildings: Multifunctional ultraviolet-shielding transparent wood. *ACS Nano* **2024**, *18*, 21288–21301.

[13] Prathap Kumar, M.; Suganya Josephine, G. A.; Tamilarasan, G.; Sivasamy, A.; Sridevi, J. Rare earth doped semiconductor nanomaterials and its photocatalytic and antimicrobial activities. *J. Environ. Chem. Eng.* **2018**, *6*, 3907–3917.

[14] Ren, Y. W.; Han, Y. J.; Li, Z. Y.; Liu, X. M.; Zhu, S. L.; Liang, Y. Q.; Yeung, K. W. K.; Wu, S. L. Ce and Er Co-doped TiO_2 for rapid bacteria-killing using visible light. *Bioact. Mater.* **2020**, *5*, 201–209.

[15] Cai, Y. Y.; Ren, W. Q.; Du, C. X.; Zhang, J. H.; Zhao, Y. X.; Yu, J. Q.; Du, H. Z.; Kang, H. Y.; Ge, X. T.; Lu, M. N. et al. Cerium oxide nanozymes: Exploring synthesis, catalytic activity, and biomedical potential. *Small* **2025**, *21*, 2504436.

[16] Liu, M. X.; Jia, Z. X.; Jia, D. M.; Zhou, C. R. Recent advance in research on halloysite nanotubes-polymer nanocomposite. *Prog. Polym. Sci.* **2014**, *39*, 1498–1525.

[17] Hoang-Minh, T.;Le, T.; Kasbohm, J.; Gieré, R. J. A. C. S. UV-protection characteristics of some clays. *Appl Clay Sci.* **2010**, *48*, 349–357

[18] Feng, Y.; Chen, X. Y.; He, R. R.; Liu, Z. Q.; Lvov, Y. M.; Liu, M. X. The horizons of medical mineralogy: Structure-bioactivity relationship and biomedical applications of halloysite nanoclay. *ACS Nano* **2024**, *18*, 20001–20026.

[19] Wu, X. K.; Li, J. L.; Jiang, Q. Y.; Zhang, W. S.; Wang, B. S.; Li, R.; Zhao, S. M.; Wang, F.; Huang, Y.; Lyu, P. et al. An all-weather radiative human body cooling textile. *Nat. Sustain.* **2023**, *6*, 1446–1454.

[20] Wang, Y. P.; Wang, Q. Q.; Wu, G. Y.; Xiang, H. X.; Innocent, M. T.; Zhai, M.; Jia, C.; Zou, P.; Zhou, J. L.; Zhu, M. F. Ultra-fast bacterial inactivation of Cu_2O@halloysite nanotubes hybrids with charge adsorption and physical piercing ability for medical protective fabrics. *J. Mater. Sci. Technol.* **2022**, *122*, 1–9.

[21] Massaro, M.; Colletti, C. G.; Lazzara, G.; Milioto, S.; Noto, R.; Riela, S. Halloysite nanotubes as support for metal-based catalysts. *J. Mater. Chem. A* **2017**, *5*, 13276–13293.

[22] Calvino, M. M.; Lisuzzo, L.; Cavallaro, G.; Lazzara, G.; Yadav, R. P.; Dolgan, K.; Lvov, Y. M. The emerging role of halloysite clay nanotube formulations in cosmetics and topical drug delivery. *ACS Appl. Bio Mater.* **2025**, *8*, 2674–2690.

[23] Zhang, Y. M.; Lu, L. J.; Xu, J.; Ning, H. Y.; Lu, L. X. Development of chitosan-based antibacterial and antioxidant bioactive film

incorporated with carvacrol-loaded modified halloysite nanotube. *Food Hydrocolloids* **2023**, *145*, 109102.
[24] Tas, B. A.; Sehit, E.; Tas, C. E.; Unal, S.; Cebeci, F. C.; Menceloglu, Y. Z.; Unal, H. Carvacrol loaded halloysite coatings for antimicrobial food packaging applications. *Food Packag. Shelf Life* **2019**, *20*, 100300.
[25] Feng, Y.; Zhang, D.; Chen, X. Y.; Zhou, C. R.; Liu, M. X. Confined-synthesis of ceria in tubular nanoclays for UV protection and anti-biofilm application. *Adv. Funct. Mater.* **2024**, *34*, 2307157.
[26] Lowe, N. J. An overview of ultraviolet radiation, sunscreens, and photo-induced dermatoses. *Dermatol. Clin.* **2006**, *24*, 9–17.
[27] Liu, X. D.; Tournassat, C.; Grangeon, S.; Kalinichev, A. G.; Takahashi, Y.; Marques Fernandes, M. Molecular-level understanding of metal ion retention in clay-rich materials. *Nat. Rev. Earth Environ.* **2022**, *3*, 461–476.
[28] Zaid, E. H. A.; Sin, J. C.; Lam, S. M.; Mohamed, A. R. Fabrication of La, Ce co-doped ZnO nanorods for improving photodegradation of methylene blue. *J. Rare Earths* **2024**, *42*, 76–83.
[29] Umar, A.; Akbar, S.; Kumar, R.; Amu-Darko, J. N. O.; Hussain, S.; Ibrahim, A. A.; Alhamami, M. A.; Almehbad, N.; Almas, T.; Seliem, A. F. Ce-doped ZnO nanostructures: A promising platform for NO_2 gas sensing. *Chemosphere* **2024**, *349*, 140838.
[30] Lang, J. H.; Wang, J. Y.; Zhang, Q.; Li, X. Y.; Han, Q.; Wei, M. B.; Sui, Y.; Wang, D. D.; Yang, J. H. Chemical precipitation synthesis and significant enhancement in photocatalytic activity of Ce-doped ZnO nanoparticles. *Ceram. Int.* **2016**, *42*, 14175–14181.
[31] Sun, M. Y.; Chen, Y. J.; Fan, X. Q.; Li, D.; Song, J. X.; Yu, K.; Zhao, Z. Electronic asymmetry of lattice oxygen sites in ZnO promotes the photocatalytic oxidative coupling of methane. *Nat. Commun.* **2024**, *15*, 9900.
[32] Fifere, N.; Airinei, A.; Timpu, D.; Rotaru, A.; Sacarescu, L.; Ursu, L. New insights into structural and magnetic properties of Ce doped ZnO nanoparticles. *J. Alloys Compd.* **2018**, *757*, 60–69.
[33] Ji, H. C.; Yu, K.; Wang, H.; Yang, H. M. Nanoclay mediated self-promoted reactive oxygen species releasing enables efficient antimicrobial. *Adv. Funct. Mater.* **2024**, *34*, 2407875.
[34] Li, G. H.; Zhong, Q. C.; Wu, W. Q.; Liu, Y. Y.; Li, H. X.; Li, X. M.; Long, T. Effect of rare earth cerium doping on the activity of ZnO nanomaterials for producing H_2O_2 by piezoelectric catalysis. *J. Colloid Interface Sci.* **2025**, *700*, 138431.
[35] Lisuzzo, L.; Hueckel, T.; Cavallaro, G.; Sacanna, S.; Lazzara, G. Pickering emulsions based on wax and halloysite nanotubes: An ecofriendly protocol for the treatment of archeological woods. *ACS Appl. Mater. Interfaces* **2021**, *13*, 1651–1661.
[36] Schroën, K.; Shen, X. F.; Hasyyati, F. I.; Deshpande, S.; van der Gucht, J. From theoretical aspects to practical food Pickering emulsions: Formation, stabilization, and complexities linked to the use of colloidal food particles. *Adv. Colloid Interface Sci.* **2024**, *334*, 103321.
[37] Boulghobra, D.; Grillet, P. E.; Laguerre, M.; Tenon, M.; Fauconnier, J.; Fança-Berthon, P.; Reboul, C.; Cazorla, O. Sinapine, but not sinapic acid, counteracts mitochondrial oxidative stress in cardiomyocytes. *Redox Biol.* **2020**, *34*, 101554.
[38] Zhao, Z. H.; Tang, C. N.; Cui, E. M.; Sun, N. N.; Zhou, J. N.; Lv, J. X.; Zhao, L.; Liu, Y. H.; Feng, S. L. Triple-scale structure-induced efficient passive radiative cooling combining robust anticondensation. *ACS Nano* **2025**, *19*, 19384–19393.
[39] Collins, P. L.; Purman, C.; Porter, S. I.; Nganga, V.; Saini, A.; Hayer, K. E.; Gurewitz, G. L.; Sleckman, B. P.; Bednarski, J. J.; Bassing, C. H. et al. DNA double-strand breaks induce H2Ax phosphorylation domains in a contact-dependent manner. *Nat. Commun.* **2020**, *11*, 3158.
[40] Dibitetto, D.; Liptay, M.; Vivalda, F.; Dogan, H.; Gogola, E.; González Fernández, M.; Duarte, A.; Schmid, J. A.; Decollogny, M.; Francica, P. et al. H2AX promotes replication fork degradation and chemosensitivity in BRCA-deficient tumours. *Nat. Commun.* **2024**, *15*, 4430
[41] Li, X. Y.; Li, Q.; He, A.; Dang, M.; Zhang, Y.; Wang, M. J.; Sun, Q. H.; Dai, Z.; Ding, M.; Zheng, J. B. et al. Disrupting biofilm tolerance by ionic microbubble-mediated copper ion surge for infection clearance. *ACS Nano* **2025**, *19*, 28624–28643.
[42] Schulze, A.; Mitterer, F.; Pombo, J. P.; Schild, S. Biofilms by bacterial human pathogens: Clinical relevance-development, composition and regulation-therapeutical strategies. *Microb. Cell* **2021**, *8*, 28–56.
[43] Yang, J. H.; Liu, K. J.; Chen, Y. Z.; Ye, H. J.; Hao, G. F.; Du, F. P.; Wang, P. Y. A supramolecular bactericidal material for preventing and treating plant-associated biofilms. *Nat. Commun.* **2025**, *16*, 2627.
[44] Ye, J.; Li, B.; Li, M.; Zheng, Y. F.; Wu, S. L.; Han, Y. Formation of a ZnO nanorods-patterned coating with strong bactericidal capability and quantitative evaluation of the contribution of nanorods-derived puncture and ROS-derived killing. *Bioact. Mater.* **2022**, *11*, 181–191.
[45] Ding, Q. H.; Ding, L. N.; Xiang, C. B.; Li, C. B.; Kim, E.; Yoon, C.; Wang, H. R.; Gu, M. J.; Zhang, P. F.; Wang, L. et al. pH-responsive AIE photosensitizers for enhanced antibacterial therapy. *Angew. Chem. , Int. Ed.* **2025**, *64*, e202506505.
[46] Zhao, F. L.; Gao, A.; Liao, Q.; Li, Y. Y.; Ullah, I.; Zhao, Y.; Ren, X. X.; Tong, L. P.; Li, X.; Zheng, Y. D. et al. Balancing the anti-bacterial and pro-osteogenic properties of Ti-based implants by partial conversion of ZnO nanorods into hybrid zinc phosphate nanostructures. *Adv. Funct. Mater.* **2024**, *34*, 2311812.
[47] Addae, A. J.; Uyanga, J.; Chifamba, J.; Weiss, P. S. Advances in enhancing photoprotection of sunscreens using hydrocarbon film formers and carbon nanomaterials. *Adv. Drug Deliv. Rev.* **2025**, *222*, 115607.
[48] Yan, X. Y.; Xu, Y. C.; Wei, T.; Chai, Y.; Li, Y. X.; Wang, C. J.; Li, M. K.; Zhang, S.; Zhu, W. J.; Liu, Z. Modified chitosan for highly efficient non-invasive transdermal delivery of catalase to repair and prevent skin photodamages. *Adv. Funct. Mater.* **2024**, *34*, 2409416.
[49] Hamanaka, R. B.; Glasauer, A.; Hoover, P.; Yang, S. N.; Blatt, H.; Mullen, A. R.; Getsios, S.; Gottardi, C. J.; DeBerardinis, R. J.; Lavker, R. M. et al. Mitochondrial reactive oxygen species promote epidermal differentiation and hair follicle development. *Sci. Signal.* **2013**, *6*, ra8.
[50] Zhang, Y. H.; Zhang, J. X.; Li, J. T.; Shen, J.; Zhang, X. F. Thermosensitive ZnO-PMMA/PEG microgels: A smart sunscreen with adapting SPF to ambient temperature fluctuations. *Mater. Today Chem.* **2024**, *37*, 102039.
[51] Fischer, T. W.; Kleszczyński, K.; Hardkop, L. H.; Kruse, N.; Zillikens, D. Melatonin enhances antioxidative enzyme gene expression (CAT, GPx, SOD), prevents their UVR-induced depletion, and protects against the formation of DNA damage (8-hydroxy-2'-deoxyguanosine) in *ex vivo* human skin. *J. Pineal Res.* **2013**, *54*, 303–312.
[52] Ahmed, N. U.; Ueda, M.; Nikaido, O.; Osawa, T.; Ichihashi, M. High levels of 8-hydroxy-2 ′ -deoxyguanosine appear in normal human epidermis after a single dose of ultraviolet radiation. *Br. J. Dermatol.* **1999**, *140*, 226–231.
[53] Hanson, K. M.; Gratton, E.; Bardeen, C. J. Sunscreen enhancement of UV-induced reactive oxygen species in the skin. *Free Radic. Biol. Med.* **2006**, *41*, 1205–1212.
[54] Han, J. L.; Colditz, G. A.; Samson, L. D.; Hunter, D. J. Polymorphisms in DNA double-strand break repair genes and skin cancer risk. *Cancer Res.* **2004**, *64*, 3009–3013.
[55] Bastien, N.; Millau, J. F.; Rouabhia, M.; Davies, R. J. H.; Drouin, R. The sunscreen agent 2-phenylbenzimidazole-5-sulfonic acid photosensitizes the formation of oxidized guanines *in cellulo* after UV-A or UV-B exposure. *J. Invest. Dermatol.* **2010**, *130*, 2463–2471.